

Numerical modelling of interactions of waves and sheared currents with a surface piercing vertical cylinder

L.F. Chen^{1, 2,*}, D. Stagonas⁶, H. Santo^{4, 5, 7}, E.V. Buldakov³, R. R. Simons³, P. H. Taylor^{2, 5}, J. Zang¹

1. WEIR Research Unit, Department of Architecture and Civil Engineering, University of Bath, Bath BA2 7AY, UK
2. Oceans Graduate School, Faculty of Engineering and Mathematical Sciences, University of Western Australia, Crawley WA 6009, Australia
3. Department of Civil, Environmental and Geomatic Engineering, University College of London, Gower St, London WC1E 6BT, UK
4. Office of the Deputy President (Research and Technology), National University of Singapore, Singapore 119077, Singapore
5. Department of Engineering Science, University of Oxford, Oxford OX1 3PJ, UK
6. Department of Mechanical Engineering, University College of London, Gower St, London WC1E 6BT, UK
7. Technology Centre for Offshore and Marine, Singapore (TCOMS), Singapore 118411, Singapore.

Highlights

- Two different approaches, 2-D OpenFOAM and Lagrangian wave-current simulations, are used to model focussed wave groups and sheared currents simultaneously in a controlled manner, and produce input conditions for 3-D OpenFOAM models to investigate wave-current-structure interactions.
- Good agreement between numerical results and experimental data is obtained, indicating that both approaches are capable of replicating experimental wave-current flows, and accurately modelling interactions between surface piercing cylinders and focussing waves on sheared currents.
- The performance of both approaches is evaluated in terms of accuracy and computational effort required.
- It is found that the method of coupling the 3-D CFD and Lagrangian models is computational slightly cheaper and more accurate because of the use of a smaller computational domain and the iterative wave-current generation in the faster Lagrangian model.

Abstract

Vertical surface piercing cylinders, such as typical coastal wind turbine foundations and basic elements of many coastal structures, are often exposed to combined loading from waves and currents. Accurate prediction of hydrodynamic loads on a vertical cylinder in a combined wave-current flow is a challenging task. This work describes and compares two different approaches for numerical modelling of the interaction between focussed wave groups and a sheared current, and then their interactions with a vertical piercing cylinder. Both approaches employ an empirical methodology to generate a wave focussed at the location of the structure in the presence of sheared currents and use OpenFOAM, an open source Computational Fluid Dynamics (CFD) package. In the first approach, the empirical wave-on-current focussing methodology is applied directly in the OpenFOAM domain, replicating the physical wave-current flume. This approach is referred to as the Direct Method. In the second approach, a novel Lagrangian model is used to calculate the free surface elevation and flow kinematics, which are then used as boundary conditions for a smaller 3-D OpenFOAM domain with shorter simulation time. This approach is referred to as the Coupling Method. The capabilities of the two numerical methods have been validated by comparing with the experimental measurements collected in a wave-current flume at UCL. The performance of both approaches is evaluated in terms of accuracy and computational effort required. It is shown that both approaches provide satisfactory predictions in terms of local free

*Emails: lifen.chen@uwa.edu.au; chenlifen239@163.com

50 surface elevation and nonlinear wave loading on the vertical cylinders with an acceptable level of
51 computational cost. The Coupling Method is more efficient because of the use of a smaller
52 computational domain and the application of the iterative wave-current generation in the faster
53 Lagrangian model. Additionally, it is shown that a Stokes-type perturbation expansion can be
54 generalized to approximate cylinder loads arising from wave groups on following and adverse sheared
55 currents, allowing estimation of the higher-order harmonic shapes and time histories from knowledge
56 of the linear components alone.

57

58 Keywords

59 Focussed wave groups; sheared currents; wave-on-current focussing methodology; Lagrangian wave-
60 current flume; Harmonic reconstruction; OpenFOAM;

61

62 1. Introduction

63 The review articles by Peregrine and Jonsson (1983a; b), Thomas and Klopman (1997) and Wolf and
64 Prandle (1999) have shown that wave-current interaction is one of the important physical processes in
65 coastal waters. The presence of a background current modifies the wave dispersion, wave-induced
66 velocities and shear stress near the seabed etc., so has an effect on wave loads on structures and wave
67 propagation near coastlines. Coastal engineering applications, such as the design of coastal protection
68 and structures as well as the evaluation of sediment transport and coastal erosion, would benefit from
69 an enhanced knowledge of this complex process and its effect on coastal structures.

70 In existing design methods, the current profile is usually assumed to be uniform with depth. The uniform
71 current approximation may apply for large-scale ocean currents and deep tidal flows, but it fails to
72 model wind-driven currents and tidal flows in shallow coastal waters that exhibit some degree of
73 variation in the vertical direction (Chakrabarti, 1996; Forristall and Cooper, 1997; Stacey et al., 1999;
74 Gunn and Stock-Williams, 2013). Previous studies demonstrated that the velocity shear modifies the
75 wave dispersion relation (Swan et al., 2001a), produces changes in water-surface elevation (Tsao, 1959;
76 Brink-Kjaer, 1976; Kishida and Sobey, 1988), and causes significant effect on the tendency of surface
77 waves to break (Peregrine and Jonsson, 1983; Yao and Hu, 2005) in a different way when compared to
78 depth-uniform currents. This work considers a current profile which varies with depth so has a
79 significant depth-varying vorticity distribution. Such a profile is a more realistic representation of a
80 current flow in some regions in the open sea.

81 The vorticity dynamics due to wave-shear current interaction can be described by the vorticity transport
82 equations, which are obtained by taking the curl of the momentum equations. Analytical solutions of
83 the vorticity transport equations exist only for the constant-vorticity case (the current is linearly sheared)
84 (Thomas, 1981; 1990; Nwogu, 2009). For more realistic profiles that vary arbitrarily with depth, the
85 computation is more difficult because of the changing vorticity field in space and time. For initially
86 uniform vorticity, Kelvin's circulation theory applies and the vorticity remains uniformly distributed.
87 Then the wave motion can be treated as an irrotational disturbance, as described by Teles Da Silva and
88 Peregrine (1988). Approximations are necessary if analytical solutions are to be sought for the cases
89 with arbitrary vorticity. Various techniques have been developed (Kirby and Chen, 1989; Swan and
90 James, 2001; Ko and Krauss, 2008; Smeltzer and Ellingsen, 2017), yet these have limited range of
91 applicability; the wave is linear or weakly nonlinear, and the current strength lies within a certain range
92 (either weak, moderate or strong). The difficulties inherent to problems associated with strongly sheared
93 currents have necessitated the use of Computational Fluid Dynamics (CFD), which is a promising tool
94 for modelling the interactions between waves and current, and both with structures.

95 Much previous numerical work based on CFD has primarily concentrated on regular wave interactions
96 with currents (Santo et al., 2017; Zhang et al., 2014; Markus et al., 2013; Li et al., 2007; Park et al.,
97 2001). However, Tromans et al. (1991) suggested the use of NewWave-type focussed wave groups as
98 design waves representing individual extreme events in random seas. Jonathan and Taylor (1997),
99 Taylor and Williams (2004), Santo et al. (2013), Christou and Ewans (2014), among others, confirmed
100 that this theory is applicable to a wide range of wave conditions. The original NewWave theory was
101 developed for deep water waves. Later it was demonstrated that it can be applied to waves on shallow
102 water (Whittaker et al., 2016). The use of NewWave-type wave groups for wave-structure interaction
103 has been demonstrated by Zang et al. (2006, 2010) for a ship-shaped fixed body and for a surface
104 piercing cylinder, respectively. Further work using wave groups on cylinders is described in the papers
105 by Fitzgerald et al. (2014) and Chen and co-workers (2014, 2016, 2018), and for jacket-type structures
106 in Santo et al. (2018).

107 Wind turbines with cylindrical foundations are likely to be located in areas with severe wave conditions,
108 with intermediate and shallow water depths and with significant currents generated by tides, storm wind
109 shear etc. Thus, the interaction of focussed wave groups propagating on either following or adverse
110 sheared currents with surface-piercing cylinders has direct practical applications.

111 The primary challenge in the numerical modelling of focussed wave groups on sheared currents is the
112 simultaneous and controlled generation of focussed wave groups on flow with non-uniform vorticity.
113 The co-existence of waves and currents alters both the evolution of the waves and the profile of the
114 currents in a way unpredictable by existing analytical approaches. As such, neither the point of focus
115 nor the elevation of the wave and the underlying flow field are known a-priori.

116 Various approaches are used to achieve wave focussing at a particular location and time in the absence
117 of currents, including a dispersive focussing method and various iterative techniques. The dispersive
118 focussing method calculates the initial phase shift of each wave component based on linear wave theory.
119 This inevitably results in a shift of the actual focus position due to non-linear wave-wave interactions
120 (Rapp and Melville, 1990; Baldock et al., 1996; Johannessen and Swan, 2001). The iterative methods
121 reconcile this issue by iteratively correcting either only the initial phases (Chaplin, 1996; Yao and Wu,
122 2005) or both the initial phases and the amplitudes (Schmittner et al., 2009; Fernandez et al., 2014;
123 Buldakov et al., 2017) of different wave frequency components in a wave group. The iterative approach
124 derived in Buldakov et al. (2017) calculates the corrected input for the wavemaker considering only the
125 linearized part of wave spectrum and therefore it differs from any previous methodology. This approach
126 has been successfully applied to physical experiments of focussed wave groups on sheared currents
127 (Stagonas et al., 2018a). The wave focussing methodologies discussed previously were mainly used in
128 physical experiments; however, its application to a numerical wave flume is straightforward and can be
129 implemented in a similar way to that in a physical flume (Stagonas et al., 2018b).

130 For either 2-D or 3-D CFD simulations, a computationally expensive fine grid is necessary to accurately
131 resolve the non-linear evolution of focussed wave groups, and the complex flow-structure interaction.
132 Applying empirical wave-on-current focussing techniques in CFD-based models, even in 2-D, may
133 yield substantial increases of the computational effort required. To accommodate this, a faster numerical
134 model may be used alternatively to produce the input wave-current kinematics for CFD-based models.
135 This work describes and compares two CFD modelling approaches building on the widely used open-
136 source CFD platform OpenFOAM. In the first approach, the wave-on-current focussing methodology
137 (Stagonas et al., 2014; 2018a; 2018b) is applied directly to a CFD numerical wave flume, replicating
138 the physical wave-current flume. 2-D simulations are performed first to calculate iteratively the
139 boundary conditions required to produce focussed wave groups on different flow conditions - namely,
140 quiescent flow without a current, adverse and following sheared current – and the interaction with the
141 structure is then modelled in 3-D. This approach is referred to as the Direct Method hereafter unless
142 otherwise stated.

143 In the second approach, a novel Lagrangian model (Buldakov et al., 2015) is coupled with the CFD
144 model. Differentiating it from recent one-way ‘online’ coupling approaches used to, e.g., model the
145 interaction of waves with cylinders (Paulsen et al. 2014a; 2014b), the time histories of the surface
146 elevation and flow kinematics are pre-computed using the Lagrangian model and are then used as inlet
147 boundary conditions for the CFD model. In this ‘offline’ coupling, all reflections are dealt by the CFD
148 simulation, eliminating the need for simultaneous computation and exchange of information between
149 the two models. This approach is referred to as the Coupling Method. We note that such a method of
150 domain decomposition, i.e. one-way coupling of simpler models with more advanced models, was also
151 applied by Biauxser et al. (2004), Drevard et al. (2005), Christensen et al. (2009), among others for
152 various flow problems but excluding the effect of flow currents. Here, the 3-D numerical flume used in
153 the Coupling Method is considerably shorter than that of the Direct Method, and the iterative wave-
154 current generation is applied in the faster Lagrangian model. The performance of both approaches is
155 validated against experimental measurements and is evaluated in terms of accuracy and computational
156 effort. The rest of the paper is organized as follows. The physical experiments on wave-sheared current-
157 cylinder interactions are described in Section 2. Details of the CFD and Lagrangian models are provided
158 in Section 3. The results of both numerical modelling methodologies are compared with the
159 experimental results in Section 4. Section 5 reconstructs the higher order harmonic forces using linear
160 components alone. Conclusions are given in Section 6.

161

162 2. Experimental setup and methodology

163 A set of experiments on wave-sheared current interactions with a vertical surface-piercing cylinder of
164 two different sizes was carried out and used to validate the proposed two CFD-based numerical models
165 in this work. This section describes the experimental setup and the applied methodology briefly.

166 2.1 Experimental setup

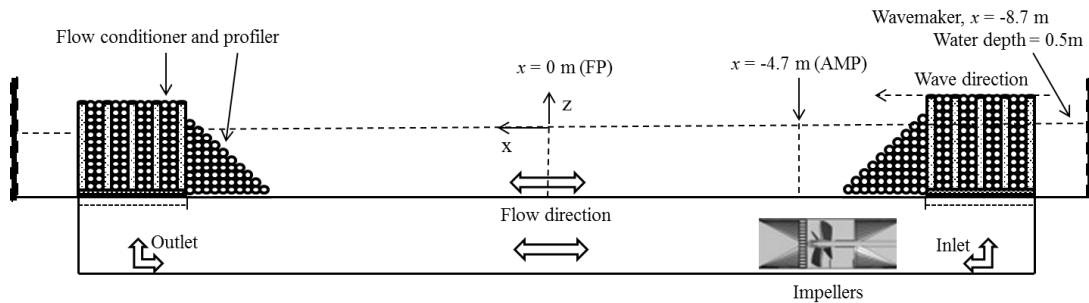
167 All experiments were conducted in a 20 m long, 1.2 m wide and 1 m deep recirculating wave-current
168 flume at University College London (UCL) with a water depth of 0.5 m. Two Edinburgh Design Limited
169 (EDL) force-feedback ‘piston-type’ wavemakers, one at each end of the facility, were used to generate
170 and actively absorb the waves. The flow entered vertically into the working section of the flume with
171 the inlet and outlet located approximately 1 m in front of each wavemaker, as shown in Figure 1. A
172 Cartesian coordinate system Oxz is introduced in both physical and numerical wave flumes such that
173 the origin O is the plane of the undisturbed free surface, $x = 0$ is the focus point, and z positive upwards.

174 The critical challenge of generating controlled and stable sheared currents was addressed through the
175 use of two carefully designed flow conditioners/profilers installed on top of the inlet and the outlet. The
176 conditioners/profilers consisted of 0.5 m long, 1.2 m wide and 0.88 m deep box sections consisting of
177 vertically and horizontally placed cylindrical elements. Each cylindrical element had a diameter of 8
178 cm and was constructed using a 5 cm porous galvanised wire mesh, see Figure 2. Compared to previous
179 work, the flow shaping approach used here has the comparative advantage of producing sheared currents
180 with variable vorticity distribution without considerable interference to the generation of waves, see for
181 example Steer et al. (2017) and for more details see Stagonas et al. (2018a).

182 Flow kinematics were measured with a high speed, time resolved Particle Image Velocimetry (PIV)
183 system produced by TSI Incorporated. The system employs a 5 W water cooled Argon Ion laser
184 operated at a pulsating frequency of 1 kHz. A light arm was used to direct the laser sheet upwards
185 through the bottom of the wave flume (the bed) and measurements were taken at the focus point (FP in
186 Figure 1) and at a distance of approximately 27 cm from the side wall; these were also the locations of
187 the free surface elevation measurements. The flow was seeded with 50 μm polyamide particles and PIV
188 images with a resolution of 1024×1024 pixels were recorded at a frame rate of 250 fps. An example of
189 the kinematics measured for adverse and following currents will be given in the following section. The
190 velocity measurements are available from still water level ($z = 0$ m) to approximately 15 cm from the

191 bed, beyond which the camera view was blocked by the support structure of the flume. Surface elevation
 192 measurements are used not only for validation but also for providing the inlet boundary conditions for
 193 the numerical models.

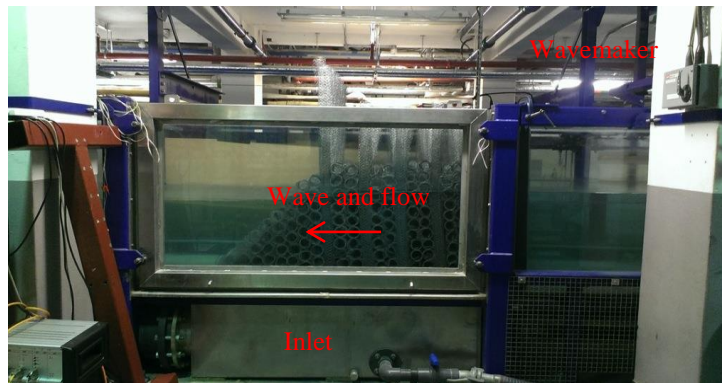
194



195

196 Figure 1. Schematic side view of the UCL wave-current flume showing two wavemakers at each end
 197 of the flume, and locations of inlet and outlet of the current discharge. FP stands for Focus Point, and
 198 AMP means the location for amplitude matching.

199



200

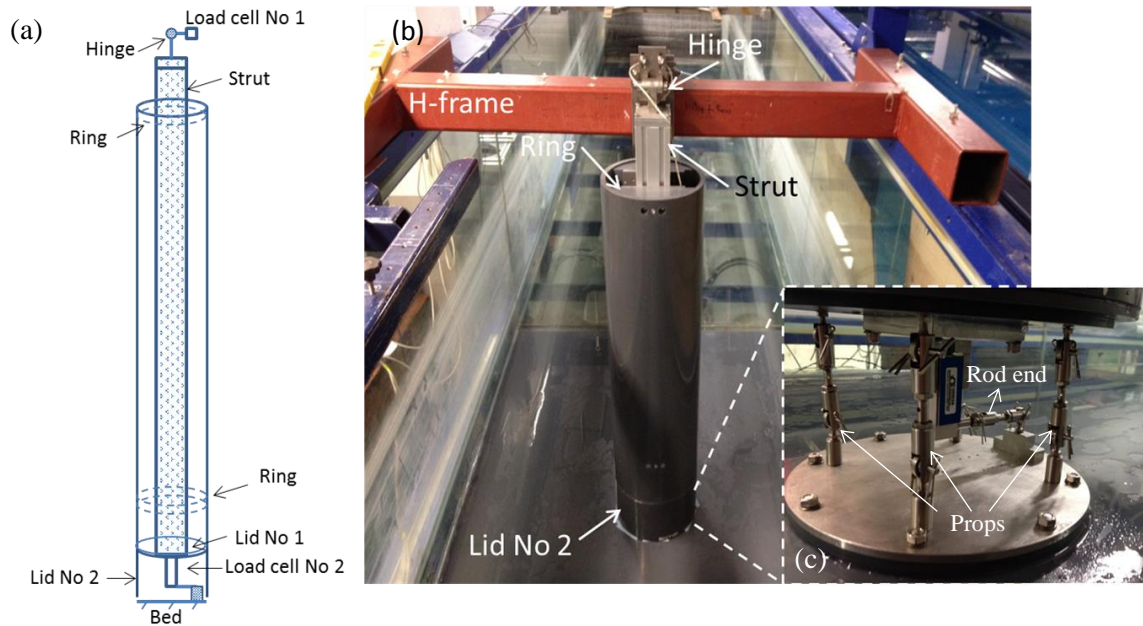
201 Figure 2 Photograph of the conditioning and profiling system

202

203 Focussed wave groups were produced using a Gaussian target spectrum on a water depth of 0.5 m. The
 204 same target spectrum was used for waves on adverse and following currents and without a current. The
 205 peak frequency was set to 0.6 Hz and the point of focus was 8.7 m from the wavemaker (FP in Figure
 206 1). The phases of different components in a wave group were forced to come to focus at the focus point
 207 and the amplitudes were matched to the target spectrum at a distance of 4 m upstream of the focus point
 208 (AMP in Figure 1). In this way, focussed wave groups with the same spectrum at a relatively short
 209 distance (1 m) from the inlet were produced for all flow conditions. The evolution to focus was
 210 measured in the physical wave-current flume using a set of wave gauges, providing the means to
 211 validate the numerical results not only at the focus point but also in terms of the evolution of the wave
 212 group along the flume.

213 Free surface elevations in the flume were measured using 7 twin-wire resistance-type wave gauges
 214 positioned at $x = -4.7$ m, -3 m, -1.8 m, -1 m, -0.5 m, -0.25 m, and 0 m, and sampled at 100 Hz. A return
 215 period of 128 s and a focus time of 64 s were selected for the wave generation. Discrete input spectra
 216 consisting of 256 frequency components with $\Delta f = 1/128$ Hz were used as input to the wavemaker. For
 217 simplicity, the wave groups produced were categorized based on the linear sum of the target amplitude
 218 components, A_L . Only the results of nonlinear wave groups with $A_L = 0.07$ m are used in the present
 219 work. The methodology employed to generate these wave groups and sheared currents both in the
 220 physical and numerical wave flumes will be described in the following subsection.

221



222

223 Figure 3 (a) Schematic diagram of side view of the cylinder model illustrating the location of the two
 224 load cells used to measure horizontal loads. (b) Photograph of the installed cylinder model. (c)
 225 Photograph showing the four props supporting the weight of the cylinder and the second/bottom load
 226 cell connected to the bed of the flume.

227

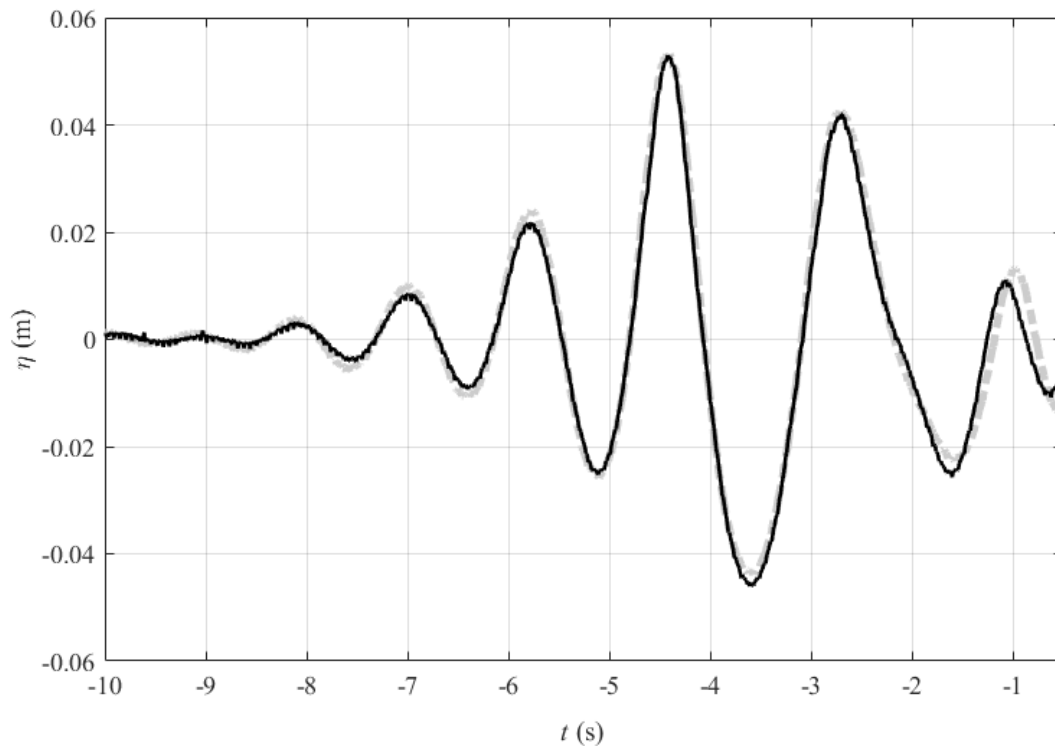
228 Experiments were also conducted with two different cylinders positioned at $x = 0$ m; for these cases an
 229 additional wave gauge was placed at the front face of the cylinder. The smaller cylinder had a diameter
 230 of 0.165 m and the larger one 0.25 m. For the smaller cylinder, flow induced loads were measured using
 231 the load cell set-up described and used in Santo et al. (2017). However, in order to more effectively
 232 support the weight of the larger cylinder, a different arrangement was developed to measure the fluid
 233 induced horizontal force. The larger cylinder was a polyvinyl chloride (PVC) tube with a diameter of
 234 $D = 0.25$ m. The PVC tube/cylinder was connected to an aluminium rectangular column, marked as
 235 'strut' in Figure 3, via circular rings. The strut had dimensions of 0.09 m (breadth) \times 0.09 m (width) \times 1
 236 m (height), and was connected to a load cell rated at 100 kg from the top through a hinge. This load cell,
 237 labelled as Load cell No 1, was rigidly fixed on the steel H-frame that was in turn tightly fixed on the
 238 flume walls. Another load cell, labelled as Load cell No 2, was located approximately 10 cm above the
 239 flume's floor and was tightly fixed on the bottom of the cylinder/strut, see Figures 3(a) and (b). The
 240 opposite end of the second load cell was connected through rod end bearings to an aluminium base,
 241 which was in turn fixed on the bed of the flume. Four props, also made using rod ends, supported the
 242 weight of the structure resulting in a preload-free cell, see Figure 3(c). The overall arrangement
 243 consisting of a strut, connecting rings and two load cells was mounted on rather than suspended from a
 244 steel H-frame. The latter arrangement was used in this study for the smaller cylinder as aforementioned
 245 and in previously reported tests by Santo et al. (2017).

246 A piece of PVC was used to model the bottom of the cylinder, labelled as Lid No 1, which was
 247 approximately 10 cm above the bed of the flume. Another piece of PVC, labelled as Lid No 2, was used
 248 to extend the model cylinder down to approximately 5 mm from the bed and compartmentalise the
 249 model cylinder, see Figures 3 (a) and (b). The compartment below the Lid No 1 was flooded and
 250 therefore a water-resistant load cell (Load cell No 2 in Figure 3) was used. Both load cells were sampled
 251 at 1 kHz and the experimental apparatus was calibrated for both tension and compression using dead
 252 weights at the beginning and the end of every testing cycle.

253 Surface elevation measurements recorded at $x = -4.7$ m (AMP in Figure 1) for different test cases
 254 illustrate a satisfactory level of repeatability. Representative results for experiments with waves on an

255 adverse current with the small (solid line) and the large (dashed line) cylinder in place are presented in
 256 Figure 4. The repeatability in load cell measurements for the same testing conditions was also tested.
 257 Standard deviations of 0.11 N/0.2 N were calculated from 15 horizontal force records acquired in
 258 consecutive repeat tests with the smaller/larger cylinder exposed to waves on the adverse current. These
 259 horizontal force results are representative of all the cases considered. It is to be noted that an iterative
 260 methodology is used in both physical and numerical wave flumes to generate focussed wave groups
 261 and sheared currents in a controlled manner. In the following sections, the iterative methodology is
 262 presented first and then the numerical flumes and implementation are described.

263



264

265 Figure 4 Example of free surface elevation time histories recorded at $x = -4.7$ m, for $U = -0.2$ m/s and
 266 $A_L = 0.07$ m. Solid line: free surface elevation profile measured with the larger cylinder installed in the
 267 flume. Dashed line: free surface elevation profile measured with the smaller cylinder installed in the
 268 flume.

269

270 2.2 Generation of focussed waves on adverse and following currents

271 A methodology to accurately generate focussed waves without a current is described in Buldakov et al.
 272 (2017) and for waves on sheared currents in Stagonas et al. (2018b). The linearized part of the wave
 273 spectrum is isolated by linearly combining four non-linear free surface elevation time histories
 274 measured in the wave flume. Initially, a crest focussed wave is produced in the flume and the remaining
 275 three wave groups are generated with phase shifts of π , $\pi/2$ and $3\pi/2$. The measured spectrum (written
 276 as a complex variable $a+ib$) is then decomposed as

277

$$\begin{aligned}
S_0 &= \frac{s_0 + s_1 + s_2 + s_3}{4} \\
S_1 &= \frac{s_0 - is_1 - s_2 + is_3}{4} \\
S_2 &= \frac{s_0 - s_1 + s_2 - s_3}{4} \\
S_3 &= \frac{s_0 + is_1 - s_2 - is_3}{4}
\end{aligned} \tag{1}$$

278 where, s_n are complex spectra of the fully nonlinear surface elevation signals with 0, $\pi/2$, π and $3\pi/2$
279 phase shifts. S_0 is the complex spectrum of the 2nd order difference components and S_1 , S_2 and S_3 are
280 complex spectra of nonlinear super-harmonics for 1st (linear), 2nd (+) and 3rd harmonic, respectively.

281 New input amplitudes are then calculated based on the measured and the target amplitudes. In the same
282 way input phases are also calculated

283

$$\begin{aligned}
a_{in}^n(f_i) &= a_{in}^{n-1}(f_i) a_{tgt}(f_i) / a_{out}^{n-1}(f_i) \\
\phi_{in}^n(f_i) &= \phi_{in}^{n-1}(f_i) + (\phi_{tgt}(f_i) - \phi_{out}^{n-1}(f_i))
\end{aligned} \tag{2}$$

284 where $a_{in}^n(f_i)$ and $\phi_{in}^n(f_i)$ are the amplitude and phase of an input spectral component at frequency f_i ,
285 respectively. $a_{out}^n(f_i)$ and $\phi_{out}^n(f_i)$ are the amplitude and phase of the corresponding spectral components
286 of the measured/recorded output spectrum, respectively. The superscript n indicates the n -th iteration.
287 $a_{tgt}(f_i)$ and $\phi_{tgt}(f_i)$ are set by the preselected target spectrum.

288 Iterations continue until the measured linearized amplitude spectrum matches the target amplitude
289 spectrum, and the phases of the linearized part are zero at the desired location in the flume. By matching
290 the measured amplitude spectrum to the target spectrum, NewWave-type focussed wave groups are
291 generated in either physical or numerical wave flumes. The methodology has also been successfully
292 applied to generate breaking waves by focussing in a CFD wave flume (Stagonas et al., 2018b) and in
293 the present work it is applied to a CFD-based numerical model and a Lagrangian numerical flume with
294 following and adverse sheared currents.

295

296 3. Numerical setup

297 Two approaches are used to replicate wave-current conditions generated in the physical flume, thus
298 providing input conditions for the 3-D CFD model with the structure in place. In the first approach, the
299 iteration scheme in physical experiments described in Section 2.2 is applied directly in the 2-D CFD
300 model, while in the second approach, a Lagrangian model (Buldakov et al., 2015) is used to provide
301 input conditions for the 3-D CFD model to reduce the size of the 3-D numerical CFD flume and shorten
302 the simulation time.

303 In this section, we first present a general description of OpenFOAM-based numerical models and then
304 the methodologies used for replicating the wave-current flow generated in the physical wave-flume are
305 detailed. The accuracy and the efficiency of the methodologies are validated by comparing with the
306 experimental measurements.

307

308 3.1 OpenFOAM-based numerical model

309 The CFD model based on OpenFOAM solves the Navier-Stokes (NS) equations or the Reynolds-
310 averaged Navier-Stokes (RANS) equations coupled with the continuity equation for the two-phase
311 combined flow of water and air with the incompressibility assumption,

312
$$\nabla \cdot \mathbf{u} = 0 \quad (3)$$

313
$$\frac{\partial \rho \mathbf{u}}{\partial t} + \nabla \cdot (\rho \mathbf{u} \mathbf{u}) - \nabla \cdot (\mu \nabla \mathbf{u}) = -\nabla p^* - \mathbf{g} \cdot X \nabla \rho + \nabla \cdot (\rho \boldsymbol{\tau}) + \sigma \kappa \nabla \alpha \quad (4)$$

314 where ρ and μ are the density and the dynamic viscosity of the mixed fluid, respectively, which are
 315 calculated following the equation (6) based on the Volume-of-Fluid (VOF) technique, which will be
 316 discussed below. $\mathbf{u} = (u, v, w)$ is the fluid velocity field in Cartesian coordinates, and p^* is the pressure
 317 in excess of hydrostatic pressure, defined as $p^* = p - (\mathbf{g} \cdot X)\rho$. \mathbf{g} is the acceleration due to gravity and $X =$
 318 (x, y, z) is the position vector. The stress tensor $\boldsymbol{\tau}$ is defined in a standard way (Jacobsen et al., 2012)
 319 and may include viscous and Reynolds stresses depending on solver settings.

320 Various turbulence closure models are implemented in OpenFOAM (e.g. Brown et al., 2016). However,
 321 the laminar flow model of OpenFOAM-2.4.0 is used in all computations reported here as both the
 322 external wave fields and the wave force on the cylinder are dominated by inertial (potential flow) effects
 323 (Chen et al., 2014; 2018). The reasonably good agreement between the numerical and experimental data
 324 shown in the following sections indicates that the consequences of viscosity and flow turbulence on the
 325 free surface elevation and wave forces on the cylinder that are of interest in this study are negligible as
 326 expected and supports the use of the laminar flow model. It is useful to note that turbulence modelling
 327 may be important if drag forces and the formation of wakes are significant (Santo et al., 2015).

328 The last term on the right-hand side of equation (4) is the effect of surface tension in which σ is the
 329 surface tension coefficient and κ is the curvature of the interface. The presence of surface tension is
 330 found to have minor effects in most civil engineering applications (Jacobsen et al., 2012; Larsen, 2018),
 331 thus, $\sigma = 0$ is used in this study.

332 The Volume-of-Fluid (VOF) technique is applied in OpenFOAM to locate and track the free surface
 333 (interface between air and water), with the following transport equation,

334
$$\frac{\partial \alpha}{\partial t} + \nabla \cdot (\alpha \mathbf{u}) + \nabla \cdot (\alpha(1-\alpha)\mathbf{u}_\alpha) = 0 \quad (5)$$

335 in which α is the volume fraction function of water within each computational cell. This equation is
 336 similar to that proposed in Hirt and Nichols (1981), but with an additional compression technique (the
 337 last term on the left-hand side in which \mathbf{u}_α is an artificial compression term) to limit the numerical
 338 diffusion of the interface profile. The compression technique is developed by OpenCFD, and details
 339 can be found in Berberovic et al. (2009).

340 The properties of the fluid at each cell are then calculated by weighting with the VOF function α , which
 341 ranges from 0 (if there is no traced fluid inside a cell) to 1 (when the cell is full of the traced fluid),

342
$$\rho = \alpha \rho_{\text{water}} + (1-\alpha) \rho_{\text{air}}; \mu = \alpha \mu_{\text{water}} + (1-\alpha) \mu_{\text{air}} \quad (6)$$

343 The equations (3) – (5) are solved with the finite volume method in which the whole computational
 344 domain is discretized into a number of cells (Ferziger et al., 2002). The merged Pressure Implicit
 345 Splitting Operator (PISO) algorithm is then applied for each cell to decouple pressure from the
 346 momentum equation (Issa, 1986).

347 Both 3-D CFD models in this study use standard implementations of boundary conditions available at
 348 OpenFOAM (with the exception of inlet and outlet boundaries which will be discussed later). Detailed
 349 descriptions of available types of OpenFOAM boundary conditions are available in Greenshields (2015).

350 We are modelling waves on sheared current by disturbing the original parallel sheared flow, which is
 351 specified by the prescribed current profile. The profile results from the current boundary layer
 352 developed on the solid bed and therefore originally satisfies no-slip conditions. Waves propagating over
 353 the current perturb the flow and lead to the development of a secondary wave boundary layer near the
 354 bed. However, we consider a fast evolving transient wave. The wave boundary layer does not have time
 355 to evolve and occupies only a very narrow region near the bed without affecting the rest of the flow.
 356 Considerable number of additional mesh points are required to resolve this layer with no considerable
 357 impact on the overall wave behaviour. We therefore using a standard OpenFOAM free-slip condition

358 with zero gradient of tangential velocity as a bed/bottom condition. This allows smooth flow behaviour
359 near the wall without high mesh resolution. The same condition is applied on the side walls.

360 We use a no-slip boundary condition on the cylinder surface, and a computational mesh near the surface
361 of the cylinder has the widths of cells ten times smaller than those away from the cylinder surface in
362 order to resolve the boundary layer. The wall-normal mesh size is selected to ensure that the
363 dimensionless wall distance (y^+) is smaller than 5 based on the flat-plate boundary layer theory. The
364 mesh dimensions for the regions away from the cylinder are determined by convergence tests to ensure
365 that there are sufficient cells per wavelength to resolve propagating incident waves and wave-current-
366 structure interactions; this will be discussed in more detail in the following section. It is found that
367 further refining the mesh inside the boundary layer has negligible influence on the flow-induced forces
368 on the cylinder. The Reynolds number $Re (= \omega \eta_m^2 / \nu)$ and the maximum local Keulegan-Carpenter
369 number $KC (= 2 \omega \eta_m / D)$ in this study are approximately 8.5×10^4 and 2.3, respectively. ω is the peak
370 wave angular frequency, ν is the kinematic viscosity and η_m is the maximum free surface elevation
371 which is about 0.15 m in this study. The initial conditions and other boundary conditions follow the
372 same set-up as described in Chen et al. (2014) and Santo et al. (2017).

373 The time step in OpenFOAM simulations is not fixed, but dynamically calculated to maintain a
374 prescribed maximum Courant number $Co = u \Delta t / \Delta x$ throughout the whole domain at all times. Δt is the
375 time step, Δx is the cell size in the direction of the velocity and u is the magnitude of the velocity at that
376 location (Courant et al., 1967). In this study an adjustable time step is used to achieve $Co = 0.25$, which
377 is again determined by numerical experimentation, and not shown here for brevity. For details refer to
378 Larsen et al. (2018).

379 OpenFOAM offers the extensive choice of numerical schemes and the iterative solvers/algorithm
380 settings for various terms in the equations (3) – (5) (Greenshields, 2015). These settings may have
381 significant effects on the performance of the CFD solvers in terms of accuracy and efficiency (Larsen
382 et al., 2018). The best choice can usually be determined from previous experience or on a case-by-case
383 basis by numerical experimentation. The scheme and solver choices used in this study are summarized
384 in Table A1 and detailed description of schemes, solvers and algorithms can be found in Greenshields
385 (2015). The combination of these choices in Table A1 has proved to work well and yield good results
386 when applied to nonlinear wave interactions with a vertical cylinder for ranges of flow conditions
387 studied in this work.

388

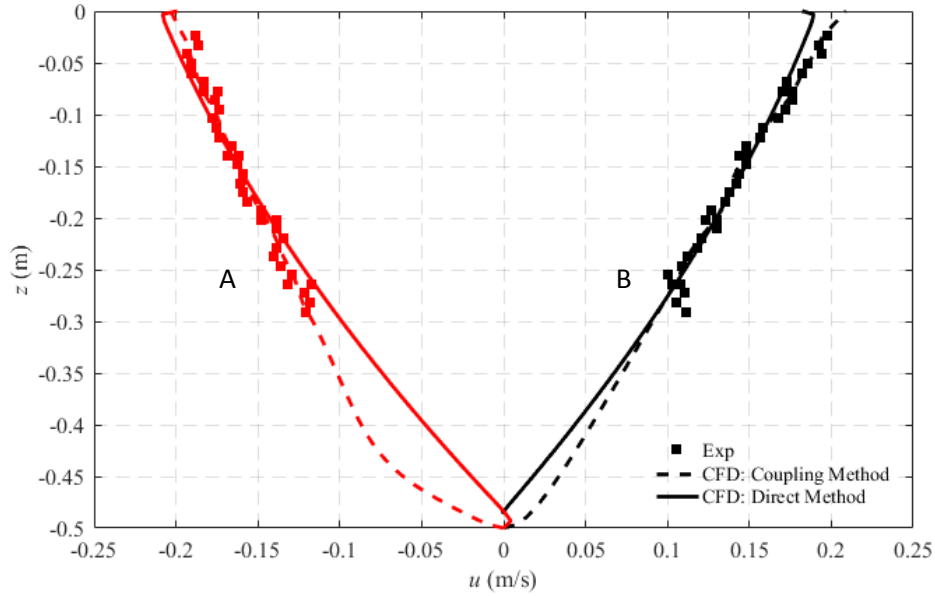
389 3.2 Direct application of the iterative wave generation methodology in CFD models

390 This study uses and extends the toolbox ‘waves2Foam’ developed and released by Jacobsen et al. (2012)
391 to realize wave generation and absorption in numerical wave flumes in OpenFOAM. The boundary
392 conditions for generating waves are given analytically according to the linear wave theory, i.e.
393 corresponding velocities and free surface elevations are specified at the input boundary faces. In this
394 study, linear superposition of velocities of the spectral components of a wave group calculated using a
395 desired spectrum (the spectrum of extracted linearized waves used here will be discussed later) is used
396 to generate the focused wave group in the computational domain through a vertical wall.

397 A new boundary condition is developed within the framework of ‘waves2Foam’ to produce a vertically
398 sheared current. The sheared current profile is defined by a second-order polynomial which is obtained
399 by curve fitting the measured horizontal velocity profile at the model cylinder location. Figure 5
400 demonstrates the current profiles used in the CFD-based numerical simulations in this paper, and their
401 comparison with measured experimental profiles.

402 The combined wave and current conditions are then generated by linearly superimposing the focussed
403 wave group and sheared current at the inlet. The boundary condition for generating sheared current is
404 also used at the outlet to ensure mass conservation.

405



406

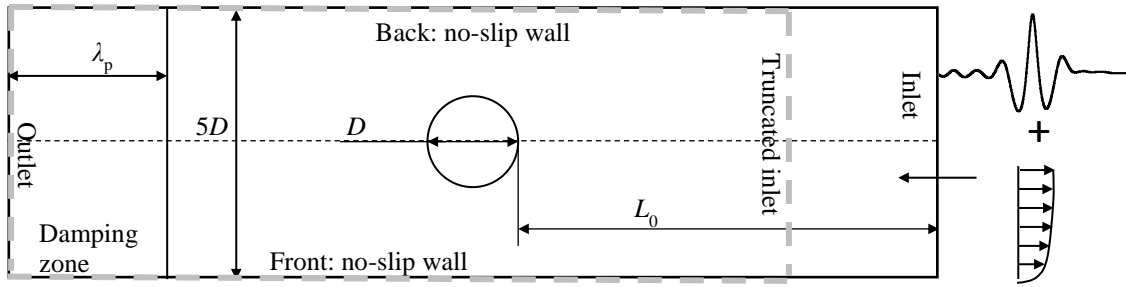
407 Figure 5 Comparisons of sheared current profile with depth obtained from the experiment and the
 408 numerical simulations at the location of the model cylinder for the cases with a sheared current and
 409 without waves. A -- Adverse current; B -- following current.

410

411 The wave-on-current focussing methodology described in Section 2.2 is now applied to generate
 412 focussed waves on various flow conditions in the numerical wave flume. All iterations are performed
 413 in a 2-D numerical flume replicating the physical flume at UCL. Although the target spectrum used in
 414 the physical wave flume can be used as inputs for the first set of simulations, the linearized spectrum
 415 extracted from the actual experimental measurements is used instead to ensure a faster convergence to
 416 the experimental measurements (i.e. $a_{in}^0 = a_{tgt} = a_{Linear}^{exp}$ and $\phi_{in}^0 = \phi_{tgt} = \phi_{Linear}^{exp}$ in equation 2). The free
 417 surface elevations at $x = -4.7$ m (AMP in Figure 1) and $x = 0$ m (FP in Figure 1) in the numerical flume
 418 are recorded and used for performing the amplitude and phase corrections following equations (1)-(2).
 419 Generally, satisfactory/convergent results for all flow conditions considered in this work are obtained
 420 within 1 or 2 iterations following the first set of simulations, i.e. in total three sets of 2-D simulations
 421 are required. The final corrected set of boundary conditions is then used as input for the 3-D numerical
 422 model shown in Figure 6. Previously, the same approach has been successfully used to simulate extreme
 423 forces induced by focussed waves on a following uniform current to a jacket structure, see Santo et al.
 424 (2018).

425 The 3-D numerical flume (which is shown in Figure 6) consists of a rectangular domain with a vertical
 426 cylinder located at the centre of the flume. The total length of the flume is 13.7 m ($\sim 4\lambda_p$) with a distance
 427 of L_0 between the inlet boundary and the vertical cylinder. The last 3 m ($\sim \lambda_p$) of the numerical flume is
 428 occupied by the relaxation zone used to minimize wave reflections from the outlet. λ_p is the peak
 429 wavelength, which is ~ 3.2 m in this study. The width of the computational domain is 1.2 m, and the
 430 water depth h is 0.5 m, the same as those in the experiments. In the Direct Method, $L_0 = 8.7$ m (~ 2.7
 431 λ_p), the same as that in the experiments.

432



433

434 Figure 6 Layout of the computational domain. D is the diameter of the vertical cylinder and λ_p is the
 435 peak wavelength. The truncated inlet demonstrates the inlet boundary for the Coupling Method; the
 436 computational flumes for the Coupling and the Direct Methods are bounded by the dashed grey lines
 437 and the solid black lines, respectively.

438

439 The optimum set-up for the computational domain including its size and the mesh resolution is
 440 determined using numerical experimentation (not shown here for brevity but more details are given in
 441 Chen et al., 2014). The principle is to have the smallest possible domain size, thus minimum
 442 computational effort, while still maintaining the correct flow field around the structure.

443 Overall, the computational domain is divided into two areas, one with a coarser and one with a finer
 444 mesh resolution. In particular, the area near the vertical cylinder and the layers near the air-water
 445 interface are resolved with a finer mesh. Horizontal and vertical grid sizes for the coarser mesh
 446 are about $\lambda_p/240$ and $H_p/12$, respectively; λ_p and H_p are the peak wavelength and the peak wave
 447 height, respectively. The cell size of the finer mesh is decreased by half, and cell sizes are graded
 448 so that the size of the cells between the two areas varies smoothly.

449

450 Table 1 Parameters and computational costs used for two OpenFOAM-based models

Parameters		Direct Method	Coupling Method
Overall length (m)		13.7 ($\sim 4\lambda_p$)	10 ($\sim 3\lambda_p$)
Overall width (m)		1.2 ($\sim 5D$)	1.2 ($\sim 5D$)
Distance from inlet to cylinder (m)		8.7 ($\sim 2.7\lambda_p$)	5 ($\sim 1.5\lambda_p$)
Distance from cylinder to outlet (m)		4.75 ($\sim 1.5\lambda_p$)	4.75 ($\sim 1.5\lambda_p$)
Length of damping (relaxation) zone (m)		3 ($\sim \lambda_p$)	3 ($\sim \lambda_p$)
Cell number (million)		~ 17.2	~ 12.6
Maximum Courant number Co		0.25	0.25
Computational costs (hrs)	Each 3-D	~ 12	~ 15.5
	Each 2-D	$\sim 1 (\times 12)^*$	--
	Total	$\sim 24^{**}$	~ 15.5

451 *In total 3 sets of 2-D simulations are required, and each set of 2-D simulations consists of 4 runs with successive
 452 additional phase shifts of $\pi/2$, in total 12 2-D simulations are required, and each 2-D simulation requires ~ 1 hour
 453 computational time.

454 **Total time is calculated as the summary of the computational time required to calculate the corrected inlet
 455 conditions using either the 2-D CFD model or the Lagrangian model and the time spent for the 3-D simulations.

456

457 The simulations were performed using the supercomputing facility at the Pawsey Supercomputing
 458 center which supports researchers in Western Australia. Utilising 48 cores for 3-D simulations, the
 459 computational time is approximately 12 hours to obtain the results within the time scale of interest, i.e.
 460 ~ 20 s of modelled time corresponding to propagation of the wave group and its interaction with the
 461 model structure. Each 2-D simulation used to calibrate the incoming wave group takes about 1 hour

462 using 24 cores. The geometric parameters used for 3-D simulations and computational costs required
 463 for both 2-D and 3-D simulations are summarized in Table 1.

464

465 3.3 Generation of the incoming wave-current flow by coupling the Lagrangian and CFD models

466 The second method of generating wave-current conditions is based on reconstructing experimental
 467 surface elevation and kinematics of incoming waves on sheared currents by applying the iterative wave
 468 generation methodology (Section 2.2) to a Lagrangian numerical wave-current flume. The Lagrangian
 469 kinematics and the free surface elevation are then fed into a truncated numerical CFD wave flume with
 470 the cylinder present using an external forcing subroutine built onto waves2Foam and OpenFOAM-
 471 based numerical models.

472 A general Lagrangian formulation for two-dimensional flow of inviscid fluid with a free surface can be
 473 found in Buldakov et al. (2006). We consider time evolution of coordinates of fluid particles $x(a, c, t)$
 474 and $z(a, c, t)$ as functions of Lagrangian labels (a, c) . The formulation includes the Lagrangian
 475 continuity equation,

$$476 \quad \frac{\partial(x, z)}{\partial(a, c)} = J(a, c), \quad (7)$$

477 the Lagrangian form of vorticity conservation,

$$478 \quad \frac{\partial(x_t, x)}{\partial(a, c)} + \frac{\partial(z_t, z)}{\partial(a, c)} = \Omega(a, c) \quad (8)$$

479 and the dynamic free-surface condition,

$$480 \quad x_{tt}x_a + z_{tt}z_a + gz_a|_{c=0} = 0. \quad (9)$$

481 Functions $J(a, c)$ and $\Omega(a, c)$ are given functions of Lagrangian coordinates and are defined by the initial
 482 conditions. $J(a, c)$ is defined by initial positions of fluid particles associated with labels (a, c) , and $\Omega(a,$
 483 $c)$ is the vorticity distribution defined by the velocity field at $t = 0$. It is convenient to select initial
 484 undisturbed positions of fluid particles as Lagrangian labels $(a, c) = (x_0, z_0)$. This gives $J = 1$. For waves
 485 over a flat bed this defines a rectangular Lagrangian domain with $c = 0$ being the free surface and $c = -$
 486 h being the bottom, where h is the undisturbed water depth. The boundary condition at the lower
 487 boundary can then be specified as,

$$488 \quad z(a, -h, t) = -h \quad (10)$$

489 The presented Lagrangian formulation offers a simple treatment of vortical flows and therefore is
 490 suitable for modelling waves on vertically sheared currents. A sheared current can be defined by
 491 specifying vorticity depending only on the vertical Lagrangian coordinate c . For our choice of
 492 Lagrangian labels the parallel current can be specified as $x = a + V(c)t$; $z = c$, where $V(c) = V(z_0)$ is the
 493 current profile. Substitution to (8) gives,

$$494 \quad \Omega(a, c) = \Omega(c) = V'(c) \quad (11)$$

495 Therefore, waves on a sheared current with an undisturbed profile $V(z_0)$ are described by equations (7,8)
 496 with the free surface boundary condition (9), the bottom condition (10) and the vorticity distribution
 497 given by (11). Figure 5 demonstrates velocity profiles for adverse and following currents we are using
 498 in this paper and their comparison with measured experimental profiles. The current profiles applied
 499 for the Coupling Method (CFD: Coupling Method in Figure 5) are obtained from PIV and ADV
 500 (Acoustic Doppler Velocimetry) measurements of the current velocity using a Bezier smoothing
 501 algorithm.

502 For convenience and efficiency of numerical realisation, we modify the original problem (7-9) and write
 503 it in the following form,

$$504 \quad \Delta_t \left(\frac{\partial(x, z)}{\partial(a, c)} \right) = 0; \Delta_t \left(\frac{\partial(x_t, x)}{\partial(a, c)} + \frac{\partial(z_t, x)}{\partial(a, c)} \right) = 0 \quad (12)$$

505 and

$$506 \quad x_{tt} x_a + z_{tt} z_a + g z_a = RHS(a, t) |_{c=0}, \quad (13)$$

507 where the operator Δ_t denotes the change between time steps and the right-hand side of the dynamic
 508 surface conditions includes various service terms. For calculations presented in this paper we use the
 509 following additional terms,

$$510 \quad RHS = \left(\frac{1}{6} \delta_a^2 x_{aa,tt} - \frac{11}{12} g \delta_t^2 z_{a,tt} \right) \quad (14)$$

$$-k(a)((x_t - V(c))x_a + z_t z_a) + P_x(a, t),$$

511 where δ_a and δ_t are the numerical mesh step in a -direction and the time discretization step. The first
 512 term in (14) is the dispersion correction term, which increases the accuracy of the numerical dispersion
 513 from second to fourth order. The second term enforces dissipation of surface perturbations. It is used
 514 for absorbing reflections, and the dissipation strength is regulated by the coefficient $k(a)$. The last term
 515 in (14) is the prescribed time varying surface pressure gradient which is used for wave generation.

516 The numerical wave-current flume is created by specifying inlet and outlet boundary conditions,
 517 distribution of surface dissipation $k(a)$ and the surface pressure gradient $P_x(a, t)$ providing free in- and
 518 outflow of the current to and from the computational domain, generation of waves on/over the current
 519 and absorption of waves reflected from domain boundaries.

520 The dissipation coefficient in the Lagrangian scheme is set to zero in the working section of the flume
 521 and gradually grows to a large value near the inlet and outlet boundaries. This results in a steady
 522 horizontal free surface at these boundaries which remain at their initial position $z = 0$ providing parallel
 523 inlet and outlet flows. This serves a double purpose. First, reflections from the boundaries are
 524 significantly reduced. Second, the boundary conditions at the inlet and outlet can be specified as the
 525 undisturbed velocity profile at the inlet and as a parallel flow at the outlet,

$$526 \quad x_t(a_{in}, c, t) = V(c); z_a(a_{out}, c, t) = 0. \quad (15)$$

527 The wave is generated by creating an area in front of one of the wave absorbers where pressure
 528 distribution of a prescribed shape is defined. Time-varying amplitude of this pressure disturbance is
 529 used as a control input for wave generation. The problem is then solved numerically using a finite-
 530 difference technique. More details of the numerical method can be found in Buldakov (2013, 2014).

531 An additional difficulty with numerical realisation of the Lagrangian formulation on sheared currents
 532 is continuous deformation of the original physical domain. The accuracy of computations for strongly
 533 deformed computational cells reduces considerably. In addition, parts of the deformed physical domain
 534 can move outside the region of interest. To avoid these difficulties, we perform sheared deformation of
 535 the Lagrangian domain to compensate for the deformation of the physical domain. The deformation
 536 takes place after several time steps and moves boundaries of the physical domain back to the original
 537 vertical lines. After this Lagrangian labels are re-assigned to new values to preserve the rectangular
 538 shape of the Lagrangian computational domain with vertical and horizontal lines of the computational
 539 grid.

540 To reproduce experimental free surface elevation records, we use the iterative procedure described in
 541 Section 2.2. Amplitudes and phases of spectral components of a pressure control signal are modified
 542 iteratively to match amplitudes and phases of the calculated linearized surface elevation spectrum at
 543 selected wave probes with target spectra. Linearized spectra of the actual experimental surface elevation
 544 at locations $x = -4.7$ m (amplitude matching position) and $x = 0$ m (focus point) are used as targets for
 545 the iterative procedure. Each numerical wave is generated with phase shifts of $n\pi/2$, with $n = 0, 1, 2, 3$.

546 This allows calculation of the linearized output signal of free surface elevation. The linearized output
547 is then compared with the target, and corrections to the input spectrum for next iteration are calculated
548 using the method described in Section 2.2. For further details of the iterative wave matching
549 methodology refer to Buldakov et al. (2017). We apply the procedure to generate incoming waves for
550 experimental cases presented in Section 2.1.

551 Lagrangian computations of the free surface elevation and flow kinematic time histories closer to the
552 structure are used as boundary conditions for a new, truncated 3-D numerical CFD wave flume (when
553 compared to the CFD domain of the Direct Method; dashed lines in Figure 6). The model cylinder is
554 centrally located in the new domain and the inlet is set at a distance of 5 m upstream from the cylinder.
555 Although Lagrangian calculations cover the full extent of the numerical flume, only the results at the
556 inlet location (truncated inlet in Figure 6) are used in the 3-D CFD model using the Coupling Method.
557 The Lagrangian results are stored every 0.025 s (40 Hz) and are linearly interpolated to match the
558 internal time step of the CFD simulation. The same outlet relaxation zone (damping zone) used in the
559 Direct Method is used in the Coupling Method to minimise wave reflection and absorb outgoing mass
560 fluxes.

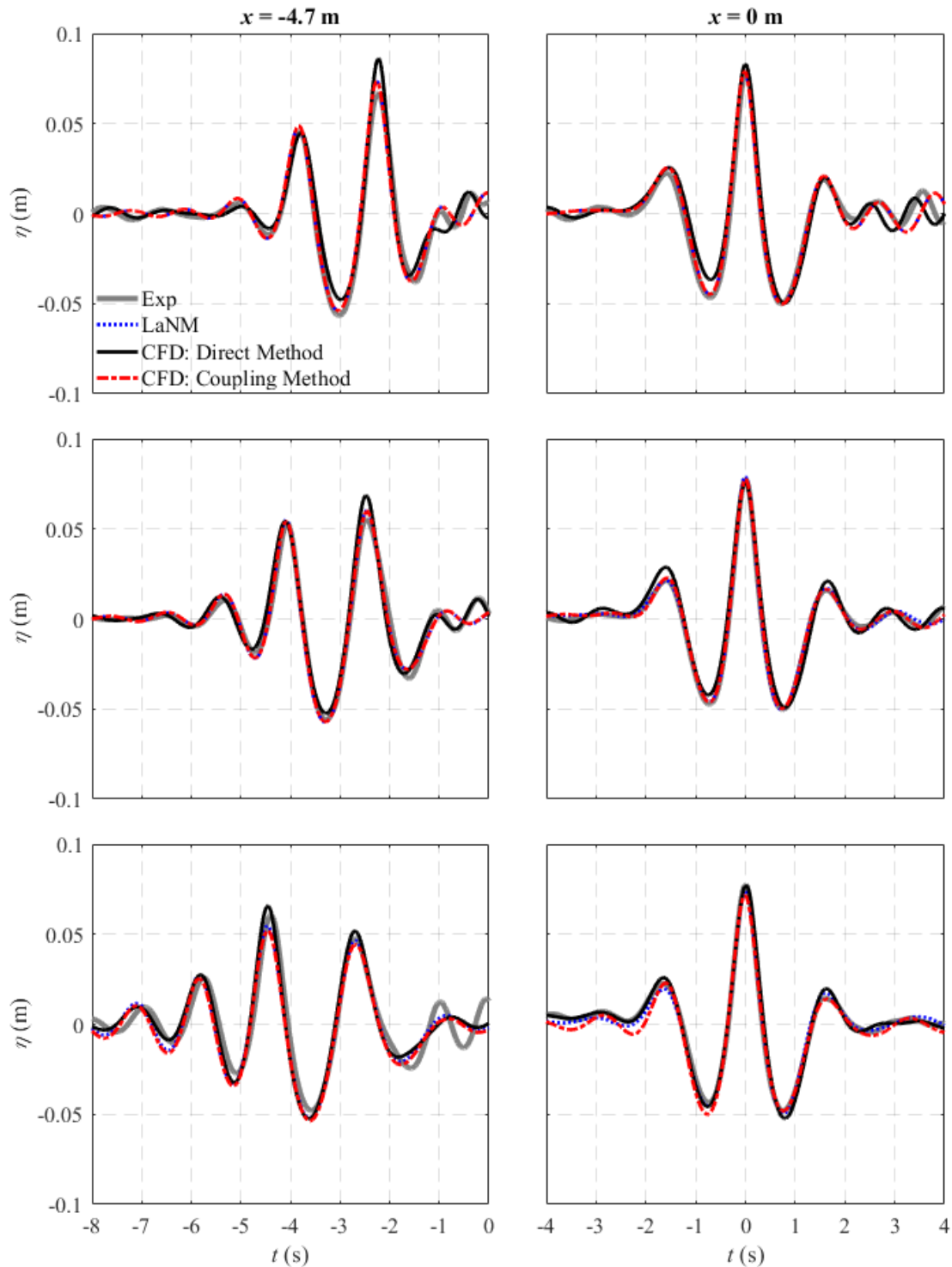
561 In contrast to the Direct Method, all iterations for the Coupling Method are conducted in the Lagrangian
562 wave flume therefore allowing for a shorter CFD wave flume. The layout of the computational domain
563 is also shown in Figure 6. Compared with the Direct Method, the distance between the (truncated) inlet
564 boundary and the vertical cylinder is now 3 m smaller with $L_0 = 5$ m, reducing total length of the
565 numerical flume from 13.7 m to 10 m. More details about the CFD domains are summarised in Table
566 1, where it is also seen that the Coupling Method is in total (including the time required for the iterations)
567 approximately 1.5 times faster than the Direct Method despite the fact that 3-D simulations with the
568 former method are found to require more computational time than simulations with the latter method.
569 This increase in computational time is attributed to the additional time required for the communications
570 between the externally provided inlet boundary conditions and the OpenFOAM model. In particular,
571 small fluctuations in inlet boundary conditions require a smaller time step to ensure the stability of the
572 simulations.

573

574 3.4 Validation of wave-current generation methods

575 The computational results with both modelling approaches for wave-current interactions without the
576 structure in place are now validated against experimental measurements. Free surface elevation time
577 histories at $x = -4.7$ m (amplitude matching position) and at $x = 0$ m (focus point) with following and
578 adverse sheared currents and without a current are presented in Figure 7. The outputs of the Lagrangian
579 numerical model are also included and are referred to as LaNM. An overall good agreement between
580 experimental results and results from both the Direct and Coupling Methods is observed, with slightly
581 larger differences being found for the Direct Method. As discussed previously, wave-current generation
582 is different between the two numerical methods (Direct and Coupling Methods) and between numerical
583 methods and experiments, and thus the generation of different spurious waves is expected. This explains
584 the main differences between the methods and between calculations and experiments. The generation
585 of spurious long waves will be discussed in more detail in the following section.

586



587

588 Figure 7 Comparisons of the free surface elevation time histories for cases with and without a sheared
 589 current. Left: $x = -4.7$ m (amplitude matching position); Right: $x = 0$ m (phase focus position). From
 590 top to bottom: following current, no current, and adverse current. All the results presented consider
 591 cases without the structure in place.

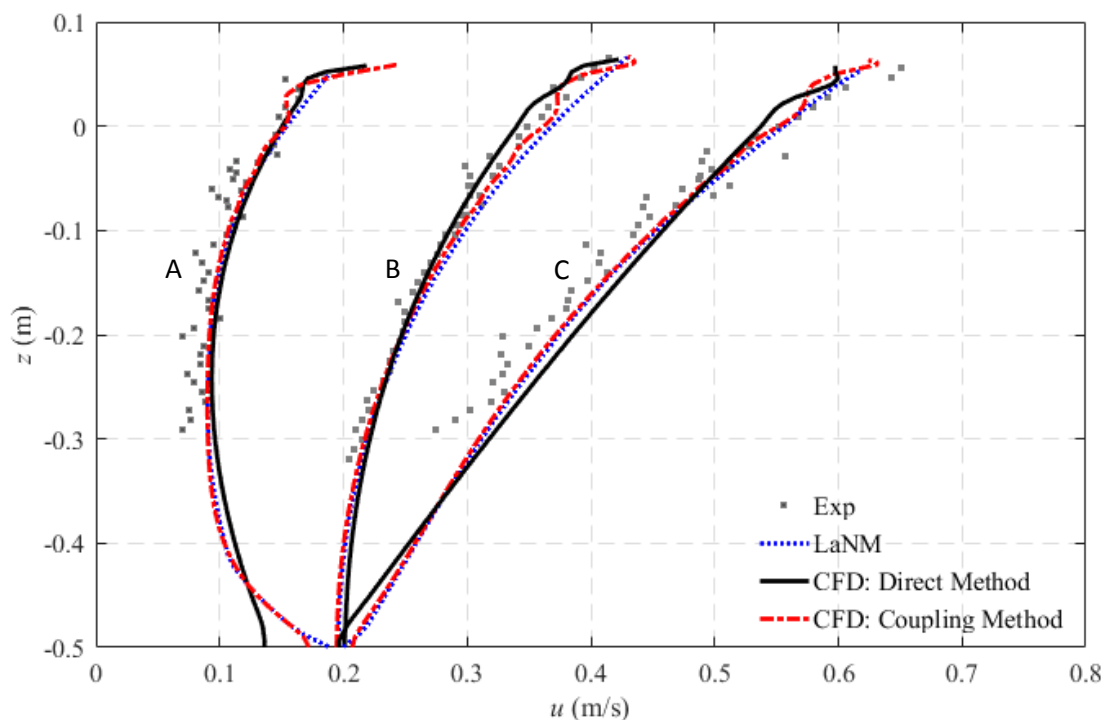
592

593 It is clear from Figure 7 that the wave shapes at the phase focussing position (right panels) for the cases
 594 with and without sheared currents are similar to each other as a result of the carefully controlled wave
 595 generation. The linearized spectrum at the focus point is the same for the experiments and computations
 596 for all the current cases considered (following, no-current and adverse current), while nonlinear
 597 contributions from higher order harmonics of the focussed wave group for different current cases are

598 rather different. This leads to the differences in the main focused wave crests and the following crests
 599 at the focussed position. Further analysis on the harmonic structure of the free surface elevation will be
 600 presented in the following section. Additionally, it can be seen that the wave shapes at the amplitude
 601 matching position (left panels) are rather different from each other for all the current cases considered.
 602 This is due to the fact that the dispersion relations are different for waves on following, zero and adverse
 603 currents.

604 Flow kinematics computed at and below the peak of the main wave crest at focus are compared with
 605 PIV measurements in Figure 8. It can be seen from Figure 8 that the two CFD models (Direct and
 606 Coupling Methods) and the Lagrangian model all provide very good predictions for the flow kinematics
 607 below still water level (0 m). The largest discrepancies between the two CFD models (Direct and
 608 Coupling Methods), the Lagrangian and experimental measurements are seen to occur in the vicinity of
 609 wave crests. This difference in the velocity profile is partly caused by the inaccuracy of the numerical
 610 velocity profile (Figure 5). The limitation of the VOF method in reconstructing very steep and sharp
 611 free-surfaces is also responsible for this difference around the interface (Wroniszewski et al., 2014).
 612 There is a sharp discontinuity of density at the interface, and the density-weighted velocity of air using
 613 the VOF factor α above the interface is close to zero, the velocity across the small interface between air
 614 and water is smeared accordingly.

615



616

617 Figure 8 Velocity profiles under the wave crest for focussed wave groups for all three cases considered.
 618 Numerical calculations and experimental measurements are included. A -- Adverse current; B -- no
 619 current; C -- following current.

620

621 4. Wave-current-structure interactions

622 Wave-current input conditions generated by the Direct Method and the Lagrangian model are now used
 623 to simulate the wave-current-structure interaction using CFD-based models. We consider six cases,
 624 including waves on following and adverse currents and without a current interacting with cylinders of
 625 two diameters $D = 0.25$ m and $D = 0.165$ m.

626 Comparisons between computed and measured time histories of the horizontal load on the cylinder and
 627 the free surface elevation at the front of the cylinder are presented in Figures 9 and 10. Results for
 628 maximum free surface elevation and peak forces are summarized in Table A2 of Appendix 2.

629 Considering the cases with the larger cylinder (Figure 9), the time histories of the non-linear elevation
 630 and horizontal force are predicted sufficiently well by either of the two approaches and the differences
 631 are observed mostly in the amplitude of the first and the main crests which are also illustrated in Figure
 632 8. The peak free surface elevation and horizontal force are generally very slightly under-predicted by
 633 both approaches.

634 An equally good comparison between experimental and numerical results is reported in Figure 10 for
 635 the cases with the smaller cylinder. Differences in computed elevations are relatively larger than those
 636 for the larger cylinder, but differences in peak force predictions are as small as those for the larger
 637 cylinder. In all six cases considered the highest discrepancies between experimental and numerical force
 638 results are seen for the cases with adverse currents and in particular for the smaller cylinder.
 639 Computational results presented so far demonstrate a sufficient capacity of both CFD approaches
 640 (Direct and Coupling Methods) to model wave-current-structure interactions.

641 In the same time, CFD model cross-comparisons, by referring to the predicted elevation and force
 642 profiles, Figures 8 and 9, and the peak elevation and force, Table A2, show a good agreement and
 643 neither of the two approaches appears to be clearly superior to the other. Nevertheless, to further explore
 644 the source of the small differences observed between computations and between both computations and
 645 measurements, the fully non-linear elevation and force time histories are decomposed into their linear
 646 and non-linear components using the methodology described in Section 2.2.

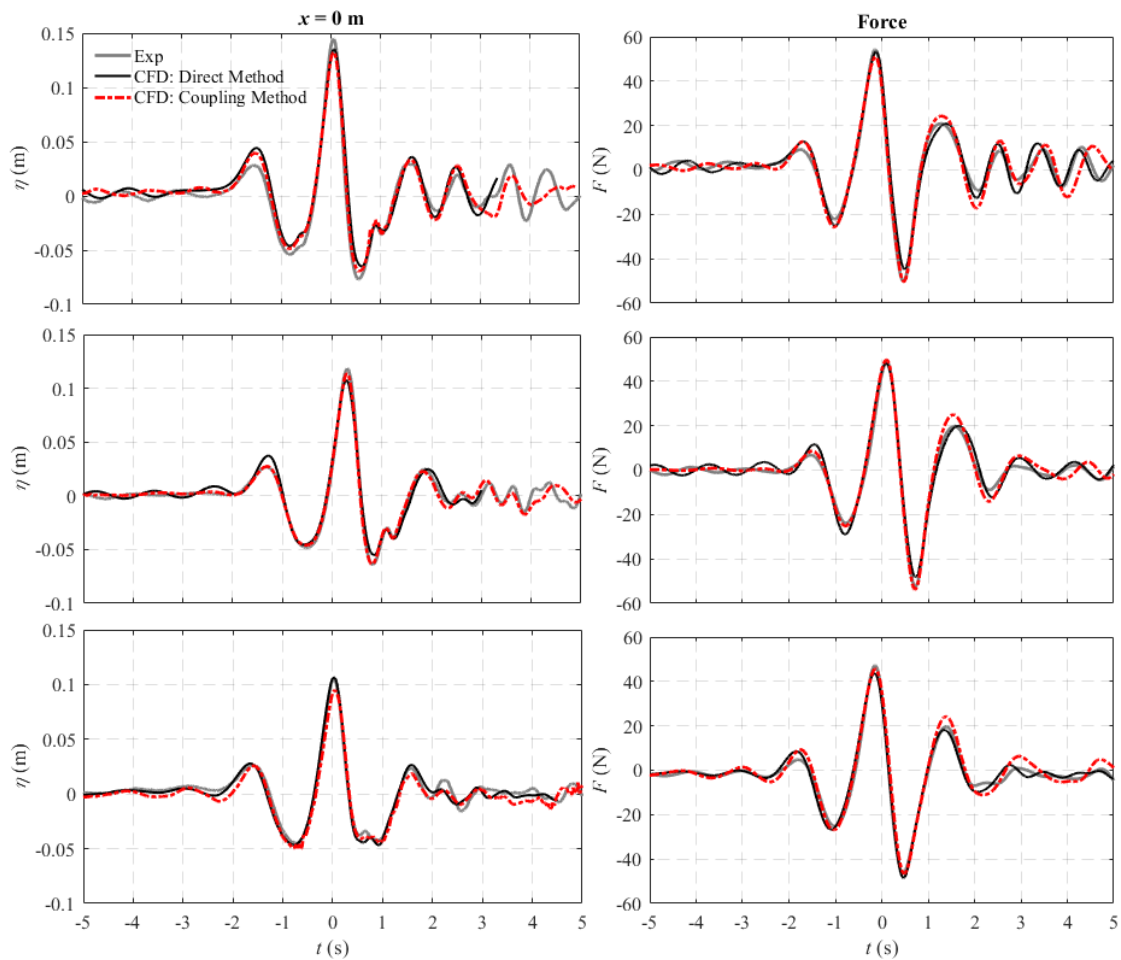
647 The decomposed spectrum and the inverse Fourier transformation of each spectral part (e.g. time
 648 histories of the 2nd order difference, linearized, 2nd order sum parts etc.) are shown in Figures 11-14.
 649 The root mean square error for each spectral part is calculated as:

$$650 \quad \text{RMSE} = \sqrt{\frac{\sum_{i=1}^N (a_{pi} - a_{mi})^2}{N}} \quad (16)$$

651 where a_{pi} and a_{mi} are the spectral amplitudes of the i^{th} ($i = 0, 1, 2, 3$) frequency predicted by the
 652 computations, and measured in the experiments, respectively. N is the number of frequencies considered
 653 in the calculations of the RMS error. N varies from 256 to 80, being larger for the linearized part and
 654 decreasing for the nonlinear part. The range of frequencies considered for calculating the RMSE is $0 <$
 655 $f/f_p < 1$ for the 2nd order difference part (S_0), $0 < f/f_p < 3$ for the linearized part (S_1), $1 < f/f_p < 3$ for the
 656 2nd order sum part (S_2), and $1.5 < f/f_p < 3.5$ for the third order part (S_3). It is noted that each frequency
 657 range was selected to include frequency components with non-negligible energy. As such, the integral
 658 spectral error calculated with equation (16) is used as an integral measure to evaluate the level of
 659 agreement between experimental and numerical results. The RMS errors for both methods and for all
 660 test cases are shown in Figures 11 to 14 and they are summarized in Table A3 of the Appendix 2.

661 Considering the 2nd order difference harmonics, discrepancies are seen in the inverse Fourier time
 662 histories of surface elevation and horizontal force on both cylinders. Given that waves are generated
 663 linearly in the physical flume the occurrence of, e.g., the 2nd order spurious wave crests at approximately
 664 $-3 \text{ s} < t < 0 \text{ s}$ in Figures 11 and 13 is not surprising. It is also worth noting that the same methodology
 665 (Section 2.2) was used to reproduce the experimental results in the Coupling Method and the Direct
 666 Method. As such, the presence of spurious wave crests in the numerical results is also not surprising.
 667 The Coupling Method is seen to somehow reproduce more closely 2nd order difference harmonics with
 668 the experimental results, especially for the tests without currents. Given the variability in wave
 669 generation methods between the flumes, and since the 2nd order wave generation is not employed, the
 670 differences in the elevation of the 2nd order difference harmonic are expected.

671 The best agreement between experimental and numerical results is observed for the linearized part of
 672 the spectra. This is an expected outcome since with the iterative methodology the computations are
 673 forced to match the linearized part extracted from the experimental spectrum. However, it is illustrated
 674 by the time histories in Figures 11 to 14 and the RMS errors in Table A3, the Coupling Method is more
 675 efficient in reproducing the experimental results.



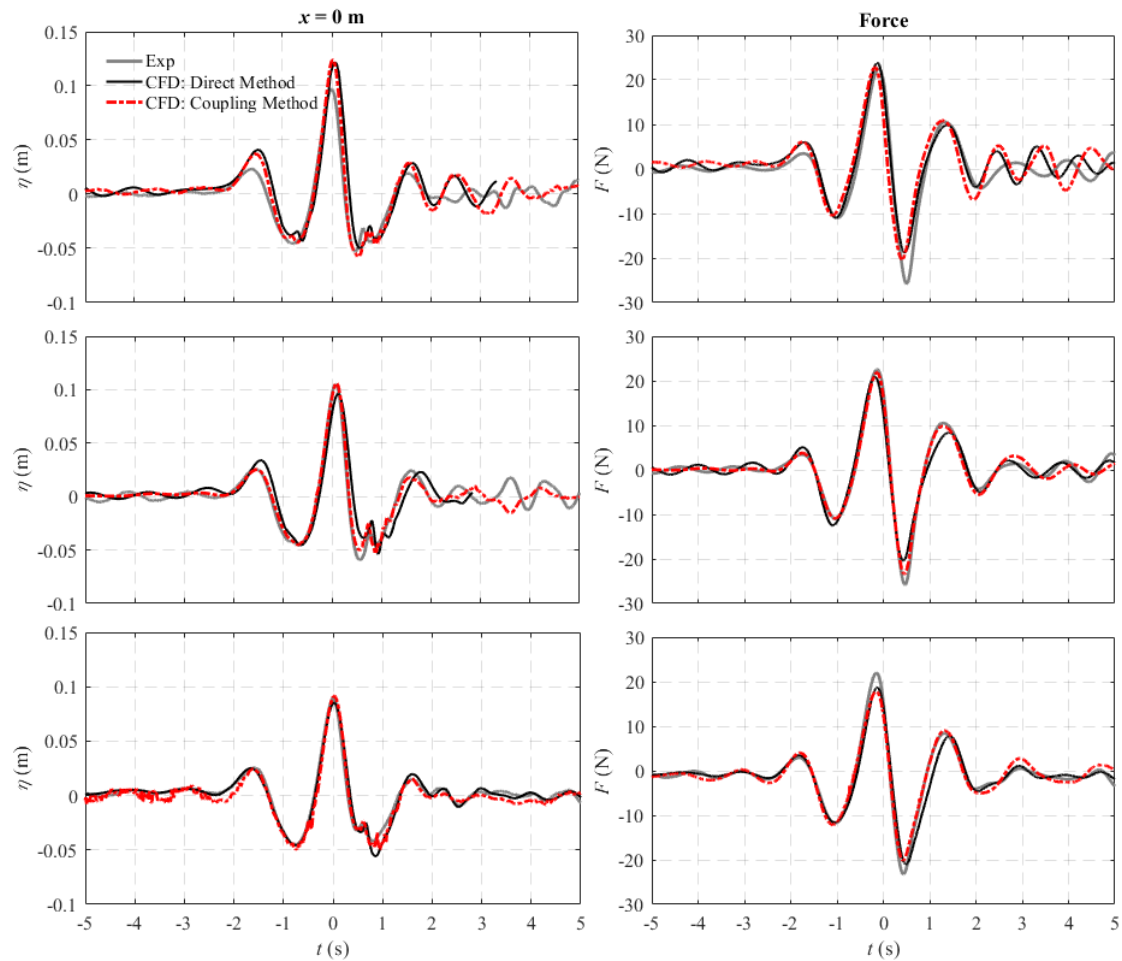
677

678 Figure 9 Comparisons of the free surface elevation time histories at the front of the cylinder (left) and
 679 the horizontal forces on the cylinder (right) for the larger cylinder ($D = 0.25$ m). From top to bottom:
 680 following current; no current; adverse current.

681

682 In contrast to spurious long waves (2^{nd} order difference harmonic), spurious short-wave components
 683 (2^{nd} order sum harmonic) travel with a celerity smaller than that of the wave group and thus they arrive
 684 at and interact with the structure after the focused wave. As a result, the agreement between
 685 experimental (elevation and force) measurements and computations for the 2^{nd} order sum harmonics
 686 improves, see for example S_2 for $-1 \text{ s} < t < 1 \text{ s}$ in Figures 11 to 14. Particularly, for tests with the smaller
 687 cylinder, the RMS error for the forces predicted by the Coupling Method is smaller but once again the
 688 difference with the errors calculated for the Direct Method is not significant.

689



690

691 Figure 10 Comparisons of the free surface elevation time histories at the front of the cylinder (left) and
 692 the horizontal forces on the cylinder (right) for the smaller cylinder ($D = 0.165$ m). From top to bottom:
 693 following current; no current; adverse current.

694

695 Similar conclusions are drawn from Figures 11 to 14 and Table A3 about the 3rd order sum harmonics
 696 albeit the agreement between the 3rd order horizontal forces is not as impressive as the agreement
 697 between experimental and numerical free surface elevation. Although the combination of four phase
 698 shifted elevation/force signals is sufficient to efficiently isolate the 3rd order harmonics (Buldakov et al.,
 699 2017), the very small amplitude of the 3rd order harmonics challenges the accuracy limits of
 700 experimental measurements. With this in mind, the performance of both Methods is considered to be
 701 satisfactory with the Coupling Method results being slightly closer to the experiments. Despite the small
 702 amplitudes, the 3rd order force harmonics are still important since they are often related to the ‘ringing’
 703 phenomenon.

704 With regards to the inter-comparison of the two numerical approaches, Figures 11 to 14 reveal no
 705 significant differences and neither model is seen to outperform the other. The small differences in the
 706 performance of the Coupling and the Direct Method are likely due to the fact that the Lagrangian model
 707 reconstructs the experimental input conditions with slightly higher precision; see also Figure 7. Small
 708 discrepancies in the 2nd order difference components can be attributed to the different wave generation
 709 methods adopted, but they are not seen to result in significant discrepancies in the overall computations
 710 of free surface elevation and force time series, e.g. Figures 9 and 10. In general, RMS errors for the
 711 Coupling Method tend to be smaller than those for the Direct Method. This in combination with the
 712 smaller computational effort required (Table 1) shows an advantage in favour of the Coupling Method.

713

714 5. Force decomposition

715 We have demonstrated in Figures 12 and 14 that the harmonic structure of forces on a cylinder in waves
 716 and sheared currents can be accurately decomposed into harmonic contributions using the four-phase
 717 based decomposition method in Section 2.2. Chen et al. (2018) showed that the harmonic structure of
 718 force on a vertical cylinder in a wave group without current can be adequately modelled based on only
 719 the linear component as follows. We write the linear component in time as

$$720 \quad F_1 = \mathcal{F}_1 f_1 \quad (17)$$

721 where \mathcal{F}_1 is the peak of the envelope of F_1 in time and f_1 carries all the phase information and group
 722 structure in time. Then the assumed form of the total force in time is

$$723 \quad \begin{aligned} \frac{F}{\rho g R^3} = & \frac{\mathcal{F}_1}{\rho g R^3} [f_1] + S_{FF2} \left(\frac{\mathcal{F}_1}{\rho g R^3} \right)^2 [\alpha_{FF2} (f_1^2 - f_{1H}^2) + \beta_{FF2} (2f_1 f_{1H})] \\ & + S_{FF3} \left(\frac{\mathcal{F}_1}{\rho g R^3} \right)^3 [\alpha_{FF3} f_1 (f_1^2 - 2f_{1H}^2) + \beta_{FF3} (f_{1H} (3f_1^2 - f_{1H}^2))] \\ & + S_{FF4} \left(\frac{\mathcal{F}_1}{\rho g R^3} \right)^4 [\alpha_{FF4} (f_1^4 - 6f_1^2 f_{1H}^2 + f_{1H}^4) + \beta_{FF4} (4f_1 f_{1H} (f_1^2 - f_{1H}^2))] + \dots \end{aligned} \quad (18)$$

724 The force approximation contains Stokes-like amplitude terms $\mathcal{F}_1 / \rho g R^3$ based on the peak amplitude
 725 of the linear force component, non-dimensional force coefficients at each order S_{FFn} and phase
 726 coefficients ($\alpha_{FFn}, \beta_{FFn}$) with $\alpha_{FFn}^2 + \beta_{FFn}^2 = 1$. $R = D/2$ is the radius of the cylinder. The subscript H
 727 denotes the Hilbert transform of the f_1 function in time, and the increasingly complicated products of f_1
 728 and f_{1H} denote the shape of the n th harmonic in time. The coefficients S_{FFn} and $\alpha_{FFn}, \beta_{FFn}$ are estimated
 729 by weighted fits, as described in Chen et al. (2018). Chen et al. (2018) showed that this approximate
 730 form works well for all the harmonics up to the 5th but that the 3rd harmonic fits are less good.

731 Here we briefly demonstrate that these decompositions work equally well for forces from waves on
 732 sheared currents, and that the form of the current affects the force coefficients S_{FFn} significantly, but the
 733 phase terms ($\alpha_{FFn}, \beta_{FFn}$) only slightly. The coefficient values are given in Table A4 of Appendix 2. We
 734 note in passing that the assumed form of the inline force on the cylinder (equation 18) neglects drag
 735 completely. Clearly, for the flow conditions reported here, unsteady inviscid components dominate the
 736 force time histories.

737 The reconstructed harmonics up to the 4th harmonic are compared to the extracted experimental
 738 harmonics in Figure 15 for the larger cylinder, and in Figure 16 for the smaller cylinder. The
 739 experimental harmonics are extracted with the four phase decomposition method of Section 2.2 and
 740 Fitzgerald et al. (2016) and the 4th sum harmonic is separated from the 2nd order difference term by
 741 digital filtering. It can be seen from the figures that the reconstructions of the 2nd and 4th harmonics
 742 work well, and for both cylinders the amplitudes of the harmonics are largest for the following current
 743 and smallest for the adverse current. These bracket the case with no current. The 3rd harmonic
 744 contributions are fitted less well with significant structure outside the time range of the (linear
 745 envelope)³ as discussed by Chen et al. (2018) for cases without current. That is, obvious wiggles outside
 746 the envelopes of 3rd harmonics are observed as shown in Figures 15 and 16; the envelopes of 3rd
 747 harmonics are approximated by raising the linear envelope to the power three, and then scaled to fit the
 748 measured envelopes of the 3rd harmonic component by a least-squares method (Chen et al., 2018).
 749 Further analysis of the forces and scattered waves is left for a follow-on paper.

750

751 6. Conclusions

752 Two approaches are proposed and used in this numerical study to generate nonlinear focussed wave
 753 groups propagating on a sheared current so as to allow an investigation of complex interactions between
 754 a combined wave-current flow and a vertical surface piercing cylinder, with applications to problems

755 in coastal engineering. Both approaches employ an iterative wave-on-current focussing methodology
756 to ensure controlled wave-current generation. In the first approach, i.e. the Direct Method, the iterative
757 methodology is applied directly in a 2-D OpenFOAM model to provide input conditions for a 3-D
758 OpenFOAM model, while in the second approach, i.e. the Coupling Method, the input wave-current
759 kinematics of the 3-D OpenFOAM model is created in a faster numerical model. In this study, a
760 Lagrangian numerical wave-current flume is used as the fast model for reconstructing experimental
761 surface elevation and kinematics of incoming focussed waves on sheared currents. There is no necessity
762 to have such a long distance between the wavemaker and the structure to ensure a full development of
763 the combined wave-current flow before the complex interactions with the structure. Thus using the
764 Coupling Method allows a smaller 3-D computational domain and shorter simulation time for modeling
765 wave-current-structure interactions when compared to the Direct Method.

766 It is worth noting that the wave-on-current focussing methodology applied in this study considers only
767 the linearized part of wave group spectrum, and phase and amplitude corrections are performed at
768 different locations to improve the effectiveness and convergence of the iterative procedure; the phases
769 are corrected at the pre-selected focus location, and amplitudes are corrected at a location well before
770 the focus position.

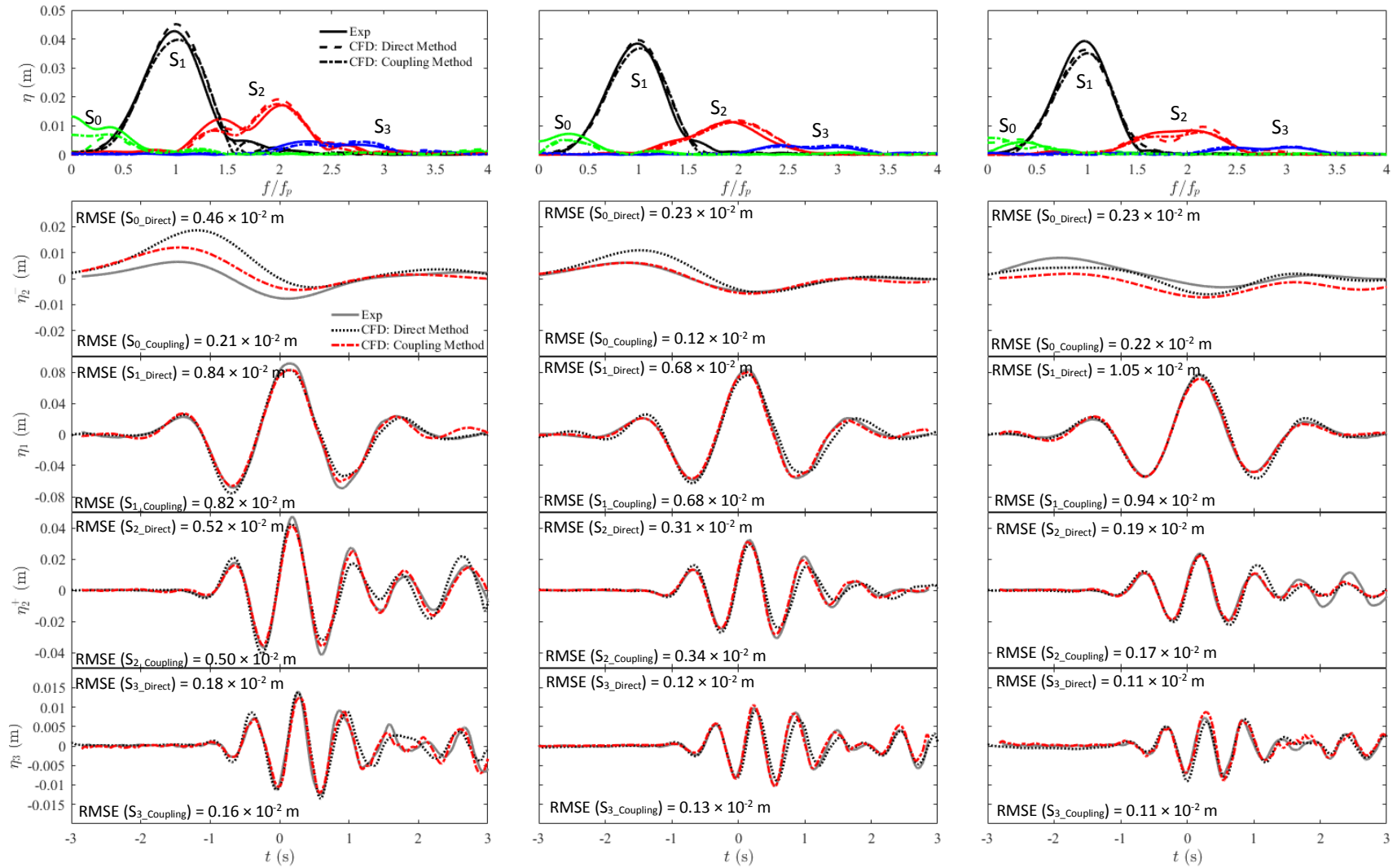
771 Good agreement between the experimental and numerical results demonstrates that both numerical
772 methods are capable of replicating experimental wave-current flows, and then accurately modelling
773 interactions between surface piercing cylinders and focussing waves on sheared currents. It is found
774 that the Coupling Method is computationally cheaper due to the application of the iterative wave-on-
775 current focusing methodology in the faster Lagrangian model. More specifically, for the simulations
776 considered in this study the computational efficiency is increased by a factor of approximately 1.5.
777 Overall, both approaches can be recommended as practical methods for studies of wave-current
778 interactions with structures, especially the Coupling Method that has a higher computational efficiency.
779 It is worth mentioning that the Lagrangian model can be coupled with various models and solvers, and
780 is thus applicable for a wide range of wave-current-structure interaction problems.

781 It is also found that the Stokes-wave perturbation expansion of Chen et al. (2018) can be generalized to
782 cylinder loads arising from wave groups on adverse and following currents and without a current. The
783 higher-order harmonic shapes can be estimated from knowledge of the linear components alone, and
784 the actual time history at each harmonic can be reconstructed to a reasonable approximation from the
785 linear component time history, using an amplitude coefficient and a phase angle at each harmonic. The
786 2nd and 4th harmonic force coefficients are found to be the largest on a following current, and the smallest
787 on an adverse current. The results for waves without a current sit in between. The 3rd harmonic forces
788 fit the simple expansion less well, as observed by Chen et al. (2018) for the case of no current. The
789 application of this reconstruction method to a wide range of wave-current conditions will be considered
790 in future work.

791

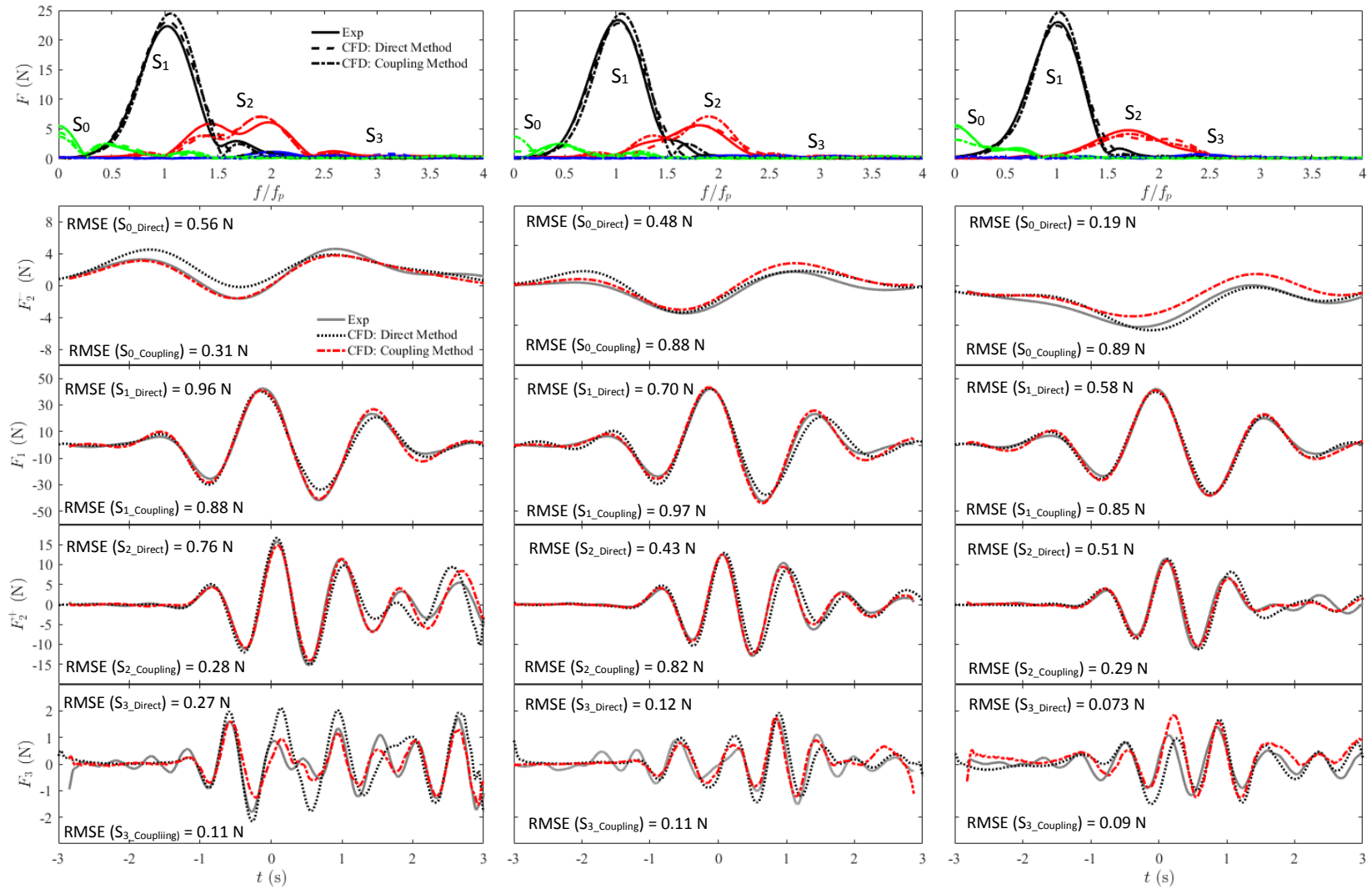
792 Acknowledgement

793 The authors thank EPSRC for providing partial support for this work within the Supergen MARine
794 Technology challenge (Grant EP/J010316/1). Resources provided by the Pawsey Supercomputing
795 Centre with funding from the Australian Government and the Government of Western Australia are
796 acknowledged. The technicians at UCL provided a high quality facility and technical service. We would
797 also like to acknowledge the use of the NUS High Performance Computing (HPC) facility and the High
798 Performance Computing (HPC) facility at the University of Bath in carrying out parts of this work.



799

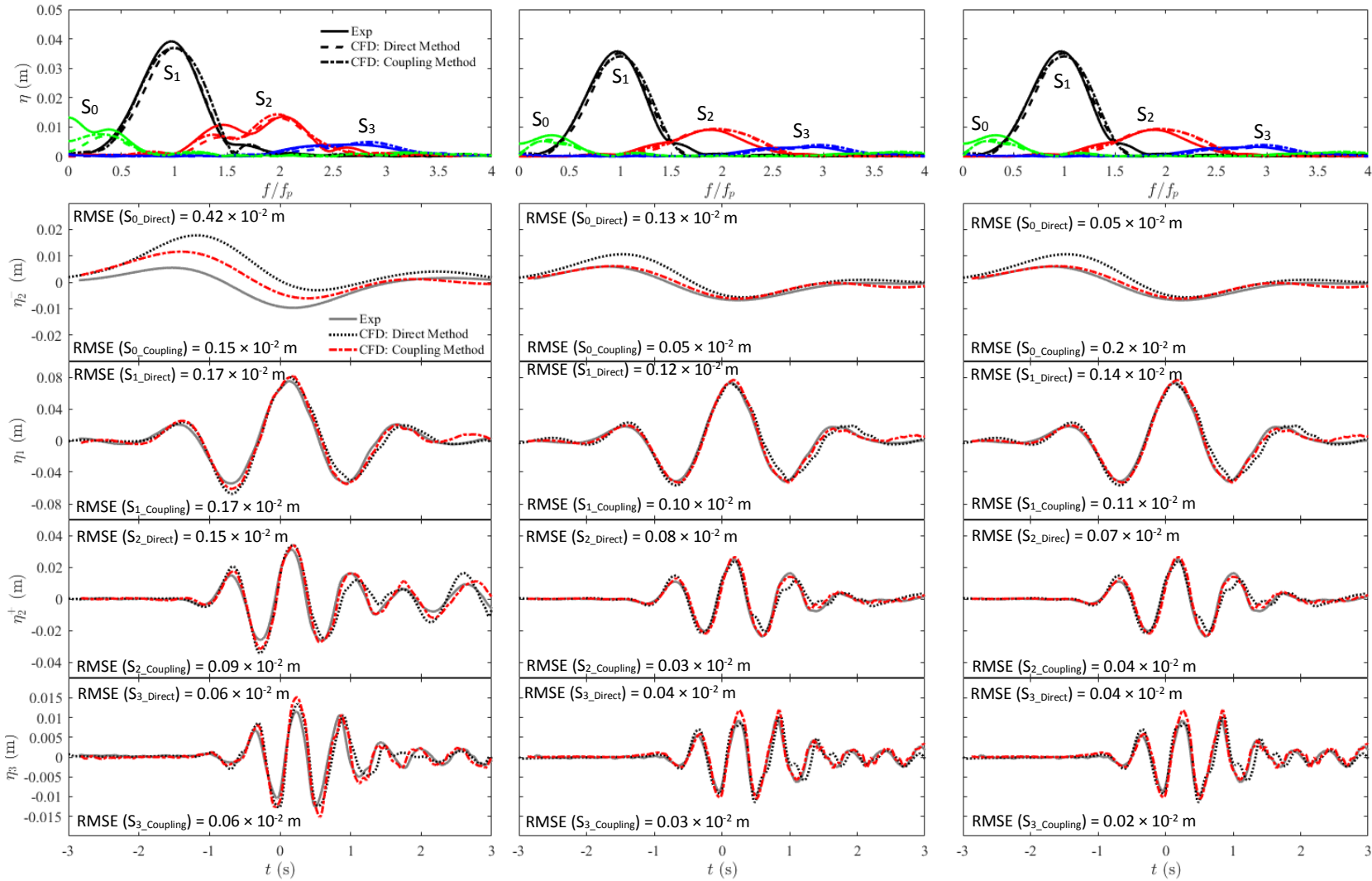
800 Figure 11 Harmonic components of the free surface elevation at the front face of the larger cylinder ($D = 0.25$ m). From top to bottom: Amplitude spectra of
 801 the free surface elevation, 2nd order difference harmonic, linear harmonic, 2nd order sum harmonic, and 3rd harmonic. From left to right: following current; no
 802 current; adverse current.



803

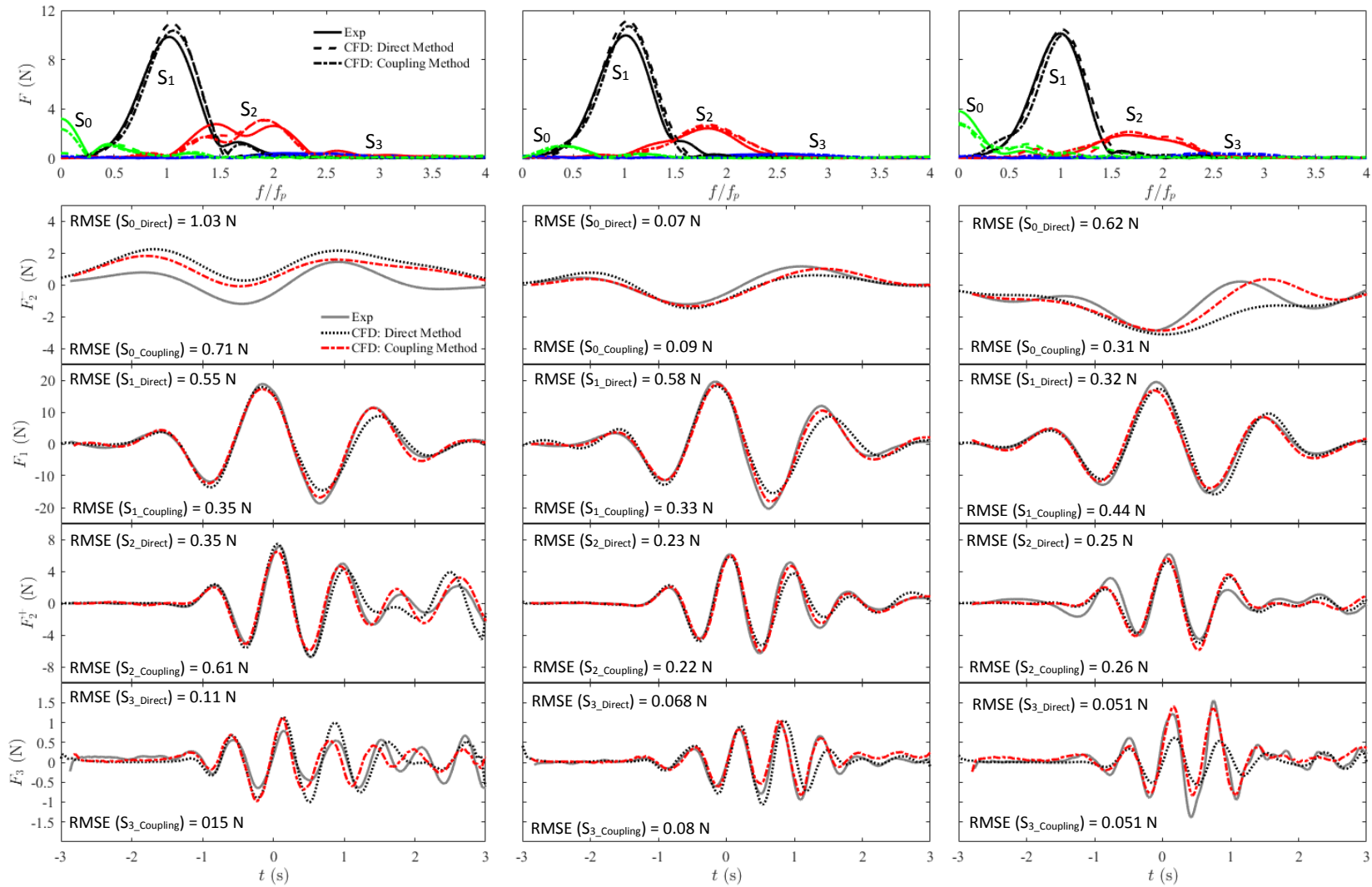
804 Figure 12 Harmonic components of the wave loading on the larger cylinder ($D = 0.25$ m). From top to bottom: Amplitude spectra of the force, 2nd order

805 difference harmonic, linear harmonic, 2nd order sum harmonic, and 3rd order harmonic. From left to right: following current; no current; adverse current.



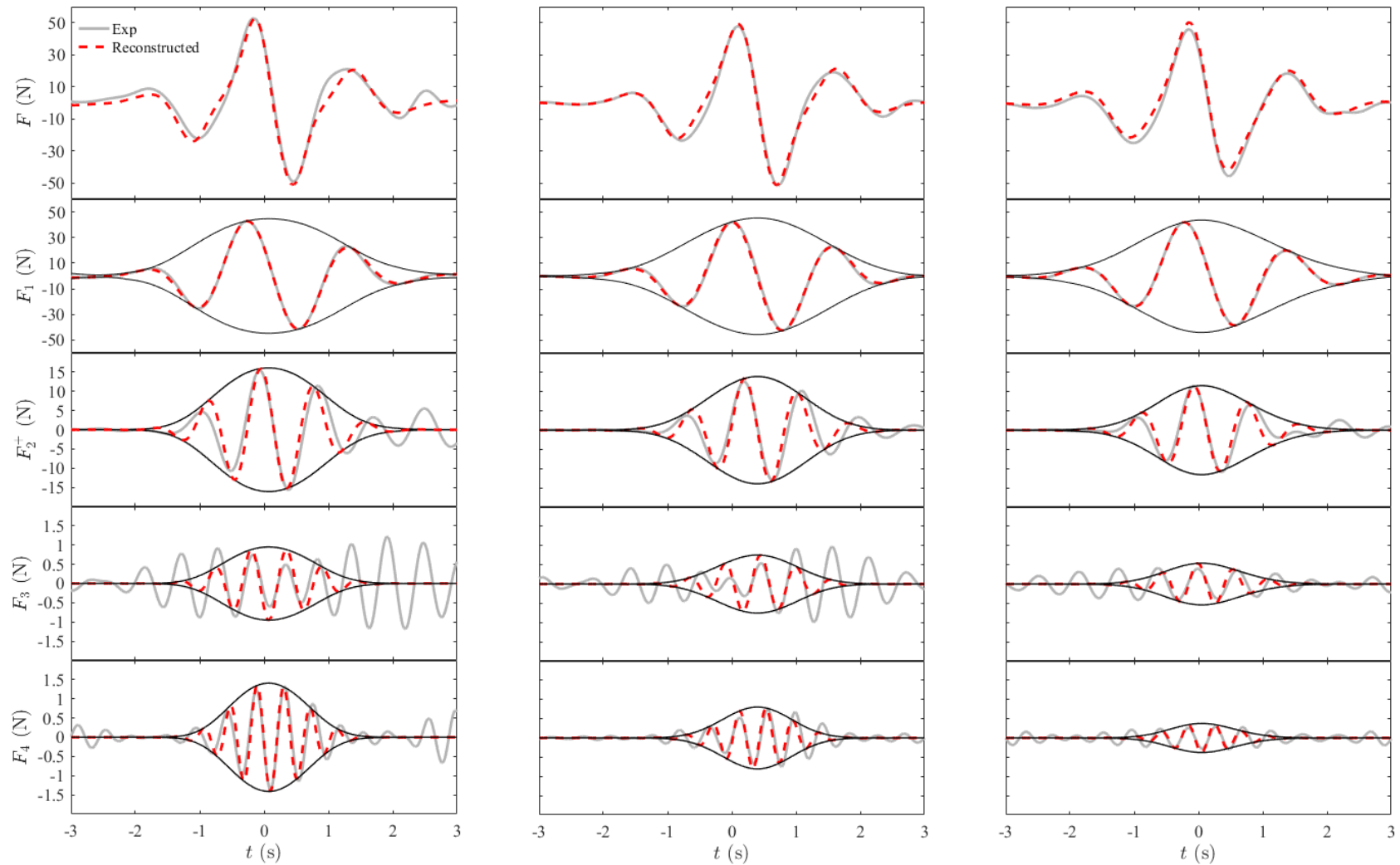
806

807 Figure 13 Harmonic components of the free surface elevation at the front face of the smaller cylinder ($D = 0.165$ m). From top to bottom: Amplitude spectra of
 808 the free surface elevation, 2nd order difference harmonic, linear harmonic, 2nd order sum harmonic, and 3rd order harmonic. From left to right: following current;
 809 no current; adverse current.



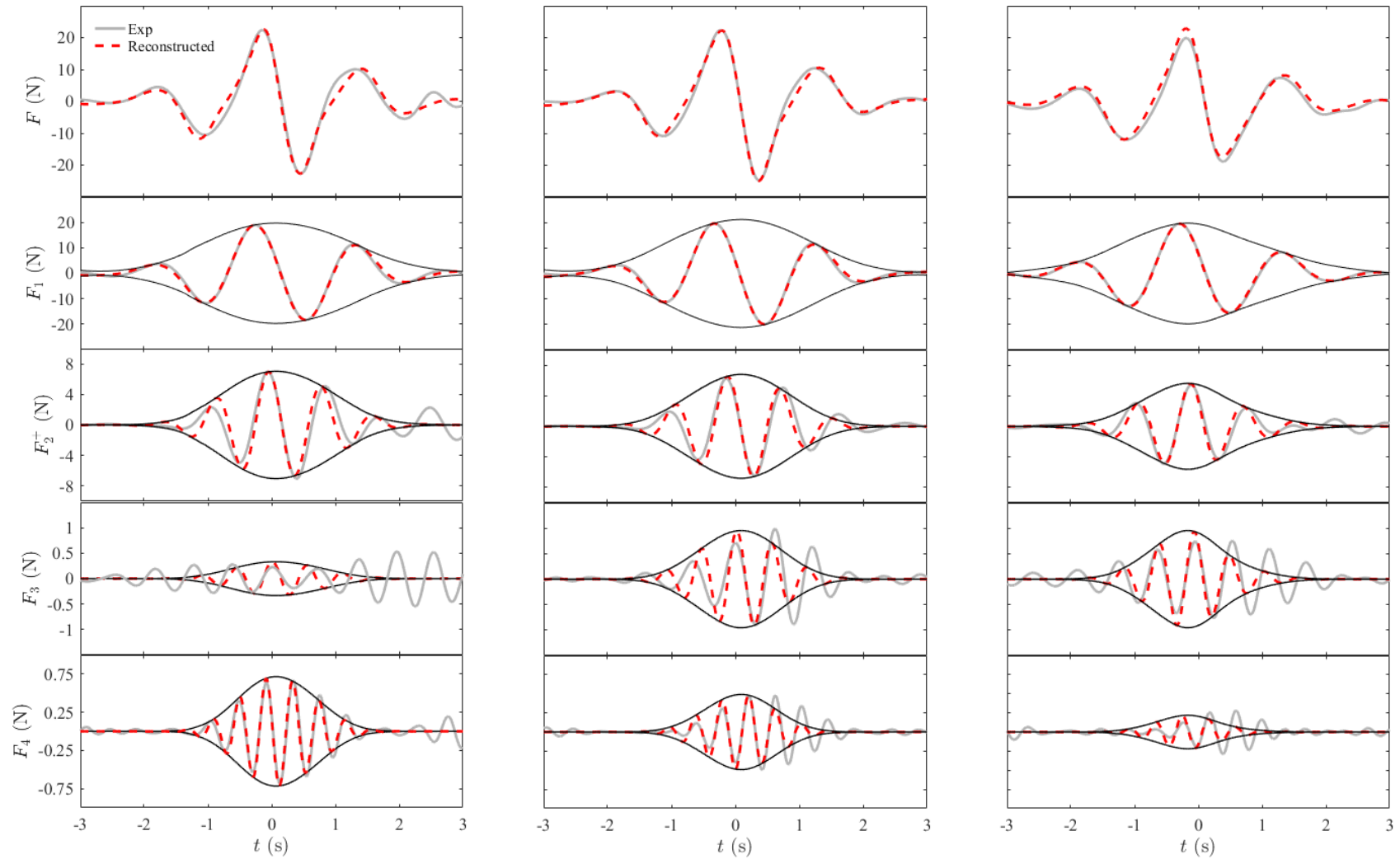
810

811 Figure 14 Harmonic components of the wave loading on the smaller cylinder ($D = 0.165$ m). From top to bottom: Amplitude spectra of the force, 2nd order
812 difference harmonic, linear harmonic, 2nd order sum harmonic, and 3rd order harmonic. From left to right: following current; no current; adverse current.



813

814 Figure 15 The reconstruction of horizontal wave loading on the larger cylinder ($D = 0.25$ m). From top to bottom: Total force, linear harmonic, 2nd order sum
 815 harmonic, 3rd order harmonic, and 4th order harmonic. From left to right: following current; no current; adverse current.



816

817 Figure 16 The reconstruction of horizontal wave loading on the smaller cylinder ($D = 0.165$ m). From top to bottom: Total force, linear harmonic, 2nd order sum
 818 harmonic, 3rd order harmonic and 4th order harmonic. From left to right: following current; no current; adverse current.

819 Appendix 1. Numerical schemes and solvers

820 The selected numerical schemes used to discretize the different terms in the governing equations, and
821 the settings for the linear solvers and for the solution algorithm are summarized in Table A1. In
822 OpenFOAM, they can be specified in the *fvSchemes* and *fvSolution* files, respectively.

823 The treatment of the first order time derivative terms ($\partial/\partial t$) in the momentum equations is specified in
824 the *ddt* scheme. Three transient schemes are widely used for engineering applications including *Euler*,
825 *Backwards* and *CrankNicolson (CN)*. The *Euler* scheme corresponds to the first-order forward Euler
826 scheme, while *Backwards* is a second-order implicit time discretization scheme in which the results
827 from the current and two previous time steps are used. A blending factor is introduced in the
828 *CrankNicolson (CN)* scheme to improve its stability and robustness; the blending factor of 1
829 corresponds to a pure *CN* scheme with a second-order accuracy, and 0 corresponds to pure *Euler*. The
830 simulations with the *Euler* scheme are faster but may lead to a heavy diffusion of the air-water interface.
831 The use of a *CN* scheme is recommended for waves with long propagation distances and times (Larsen
832 et al., 2018).

833 One of major challenges in CFD calculations is the treatment of convective/advective terms in the
834 governing equations. Different schemes are specified for different convective terms as they are
835 fundamentally different. The standard finite volume discretization of Gaussian integration is
836 implemented in OpenFOAM in which the integral over a control volume is converted to a surface
837 integral using the Gauss theorem. Accordingly, the word “*Gauss*” is specified in the numerical schemes.
838 The Gaussian integration requires the interpolation of the field variable from cell centres to face centres
839 using for example central/linear or upwind differencing. The former is second-order accurate, but may
840 cause oscillations (unboundedness) in the solution, while the latter is first order accurate, thus, is more
841 diffusive. In lieu of this, various total variation diminishing (TVD) and normalized variable diagram
842 (NVD) schemes that utilize combined upwind and linear differencing are implemented in OpenFOAM,
843 including schemes of *limitedLinear* and *vanLeer*. The use of upwind differencing or linear upwind
844 differencing for the momentum flux is preferable if the loads on the structure are of main concern, such
845 as the cases in this study. A similar conclusion is presented in Larsen et al. (2018).

846 Generally, the linear schemes are used for calculating the gradients and the interpolation from cell
847 centres to face centres although higher order accurate schemes are available. The *laplacian* scheme
848 requires the specification of an interpolation scheme for e.g. the dynamic viscosity μ , and a surface
849 normal gradient scheme for e.g. $\nabla \mathbf{u}$. Again, linear schemes are often used with orthogonality corrections
850 for surface normal gradients. For more detailed descriptions on various numerical schemes in
851 OpenFOAM, the reader is referred to the OpenFOAM user’s guide (Greenshields, 2015) and
852 programmer’s guide (Greenshields, 2015) as well as Larsen et al. (2018).

853 The iterative solvers, solution tolerances and algorithm settings for solving the discretised algebraic
854 equations are specified in the *fvSolution* file. Various iterative solvers are implemented in OpenFOAM,
855 including preconditioned (bi-) conjugate gradient solvers (PCG/PBiCG) and *smoothSolver* in which the
856 specification of preconditioning of matrices (preconditioner) and smoother is required, respectively.
857 The generalised geometric-algebraic multi-grid (GAMG) solver is also commonly used in which the
858 initial guess of the accurate solution on the finer simulation mesh is obtained by mapping the quicker
859 solutions on a coarser mesh to this finer mesh. Generally, the GAMG solver is quicker than the
860 *smoothSolver*, whereas the latter may yield more accurate results. The use of PCG/PBiCG solver sits
861 in between. Detailed descriptions refer to the OpenFOAM user’s and programmer’s guides (2015).

862 In this study, the compression velocity \mathbf{u}_a in the equation (5) equals to the flow velocity at the interface
863 by specifying *cAlpha* to be 1. A larger value of *cAlpha* leads to a sharper interface but also the
864 appearance of wiggles in the air-water interface which is found to be responsible for un-physical
865 steepening of waves and over-estimations of wave celerity (Larsen et al., 2018). Whereas, the use of a

866 smaller $cAlpha$ reduces the wiggles but at the same time leads to a more significant smearing interface.
 867 Another two important controls over the α equation are $nAlphaCorr$ and $nAlphaSubCycles$; the former
 868 specifies how many times the α field should be solved within a time step, and the latter represents the
 869 number of sub-cycles for the α equation within a given time step.

870 As aforementioned, the PISO algorithm is applied in this study, thus, $nOuterCorrectors = 1$, and the
 871 parameter $nCorrectors$ is the number of pressure corrector iterations in the PISO loop and the
 872 $momentumPredictor$ is a switch that controls solving of the momentum predictor. Each time step will
 873 be begun by solving the momentum equation rather than the pressure equation if the momentum
 874 predictor is turned on.

875

Numerical schemes			
Terms in equations	Representation in OpenFOAM	Discretization schemes	Description
Time derivatives	ddt	Euler	First order forward Euler scheme
Gradients	grad	Gauss linear	--
Divergence (momentum flux)	div(rho*phi, U)	Gauss linearUpwind, grad(U)	Second order, upwind-biased, specification of velocity gradient is required.
Divergence (mass flux)	div(phi, alpha)	Gauss vanLeer	Total variation diminishing (TVD)
Divergence	div (phib, alpha)	Gauss linear	--
Laplacian	laplacian	Gauss linear corrected	Interpolation and snGrad schemes are required.
Interpolation	interpolation	linear	--
Surface normal gradient	snGrad	corrected	Linear with orthogonality correction
Iterative solvers			
Equations	Variable field	Solvers	Left to right are: solver, preconditioner/smoothen, tolerance, relative tolerance
Pressure p^*	pcorr/p_rgh/ p_rghFinal	PCG, DIG, 1e-5, 0	
Velocity U	U	smoothSolvers, symGaussSeidel, 1e-06, 0	
VOF function α	alpha.water	smoothSolvers, symGaussSeidel, 1e-08, 0	
Algorithm controls			
Artificial compression term u_α	cAlpha	1	$u_\alpha = u$ in which u is the flow velocity at the interface
PISO loop	momentumPredictor	no	Loop starts by solving the pressure equation
PIMPLE loop	nOuterCorrectors	1	PISO is used, otherwise, PIMPLE is used.
PISO loop	nCorrectors	3	pressure corrector iterations
Loop over the α equation	nAlphaCorr	2	α corrector iterations
	nAlphaSubCycles	1	Number of sub-cycles

876 Table A1 The selected numerical schemes and iterative solvers.

877 Appendix 2. Detailed model comparisons and coefficients used for the reconstruction

878 Table A2 summarized the results for maximum surface elevation and peak forces, and all differences
 879 in Table A2 are calculated with respect to the experimental data and they are only used for a qualitative
 880 model comparison. Integral spectra errors are reported in Table A3 and used as an approach
 881 demonstrating model accuracy in depth. Table A4 summarized the coefficients used for reconstructing
 882 the higher order harmonics from the linear components alone, as shown in Figures 15-16.

883

884 Table A2 Comparisons between the two models in terms of wave crests/troughs and peak forces

Cylinders	Cases		Exp.	Direct Method		Coupling Method	
	Parameters	Current (Heading)		Num.	Differences (%)	Num.	Differences (%)
$D = 0.25$ m	Wave crest (m)	Following	0.144	0.135	-6	0.135	-6
		No current	0.118	0.108	-8	0.114	-3
		Adverse	0.107	0.107	0	0.093	-13
	Wave trough (m)	Following	-0.077	-0.065	-16	-0.070	-9
		No current	-0.064	-0.055	-14	-0.061	-5
		Adverse	-0.042	-0.046	10	-0.043	2
	Positive peak forces (N)	Following	54.17	53.07	-2	52.67	-3
		No current	48.10	48.10	0	49.70	3
		Adverse	46.90	43.89	-6	45.46	-3
	Negative peak forces (N)	Following	-49.04	-44.75	-9	-48.90	0
		No current	-51.25	-48.07	-6	-53.63	5
		Adverse	-46.03	-48.33	5	-44.94	-2
$D = 0.165$ m	Wave Crest (m)	Following	0.100	0.120	20	0.120	20
		No current	0.105	0.096	-9	0.105	0
		Adverse	0.090	0.085	-6	0.091	1
	Wave trough (m)	Following	-0.053	-0.049	-8	-0.055	4
		No current	-0.059	-0.054	-8	-0.051	-14
		Adverse	-0.040	-0.055	38	-0.047	18
	Positive peak forces (N)	Following	22.51	23.84	6	22.51	0
		No current	22.51	20.93	-7	21.69	-4
		Adverse	22.00	18.28	-17	18.28	-17
	Negative peak forces (N)	Following	-24.53	-18.67	-24	-20.17	-18
		No current	-25.71	-19.66	-24	-22.64	-12
		Adverse	-23.04	-20.9	-9	-19.90	-14

885

886 Table A3 Root-mean-square errors for various harmonics in spectra space

Cases			Direct Method				Coupling Method			
Cylinders	Parameters	Current (Heading)	2 nd order dif.	Linearized	2 nd order sum	3 rd order	2 nd order dif.	linearized	2 nd order sum	3 rd order
$D = 0.25$ m	Free surface elevations ($\times 10^{-2}$ m)	Following	0.46	0.84	0.52	0.18	0.21	0.82	0.50	0.16
		No current	0.23	0.68	0.31	0.12	0.12	0.68	0.34	0.13
		Adverse	0.23	1.05	0.19	0.11	0.22	0.94	0.17	0.11
	Forces (N)	Following	0.56	0.96	0.76	0.27	0.31	0.88	0.28	0.11
		No current	0.48	0.70	0.43	0.12	0.88	0.97	0.82	0.11
		Adverse	0.19	0.58	0.51	0.073	0.89	0.85	0.29	0.09
$D = 0.165$ m	Free surface elevations ($\times 10^{-2}$ m)	Following	0.42	0.17	0.15	0.06	0.15	0.17	0.09	0.06
		No current	0.13	0.12	0.08	0.04	0.05	0.10	0.03	0.03
		Adverse	0.05	0.14	0.07	0.04	0.2	0.11	0.04	0.02
	Forces (N)	Following	1.03	0.55	0.35	0.11	0.71	0.35	0.61	0.15
		No current	0.07	0.58	0.23	0.068	0.09	0.33	0.22	0.08
		Adverse	0.62	0.32	0.25	0.051	0.31	0.44	0.26	0.051

887

888 Table A4 Coefficients for reconstructing the higher order harmonics for all three flow conditions

kR	kh		Order	Coefficients		
				Following	No current	Adverse
0.242 (larger cylinder)	0.97	Amplitude (S_{FFn})	2	3.03	2.58	2.06
			3	0.34	0.27	0.18
			4	0.98	0.54	0.23
		Phase (deg.) ($\alpha_{FFn}, \beta_{FFn}$)*	2	97	94	73
			3	49	305	148
			4	145	123	68
0.160 (smaller cylinder)	0.97	Amplitude (S_{FFn})	2	2.01	1.89	1.51
			3	0.12	0.34	0.32
			4	0.33	0.22	0.09
		Phase (deg.) ($\alpha_{FFn}, \beta_{FFn}$)*	2	99	99	81
			3	183	245	190
			4	165	128	48

889 * Phase = $\arctan(\beta_{FFn} / \alpha_{FFn})$

890

891 References

- 892 Baldock, T., Swan, C., Taylor, P.H., 1996. A laboratory study of nonlinear surface waves on water.
 893 Philos. Trans. Roy. Soc. A Math. Phys. Eng. Sci. 354 (1707), 649-676.
- 894 Berberović, E., van Hinsberg, N.P., Jakirlić, S., Roisman, I.V., Tropea, C., 2009. Drop impact onto a
 895 liquid layer of finite thickness: dynamics of the cavity evolution. Phys Rev E - Stat Nonlinear Soft
 896 Matter Phys. 79(3), 036306.
- 897 Biauxser, B., Fraunie, P., Grilli, S.T., Marcer, R., 2004. Numerical analysis of the internal kinematics
 898 and dynamics of 3-D breaking waves on slopes. Int. J. Offshore Polar Eng. 14, 247–256.
- 899 Brink-Kjaer, O., 1976. Gravity waves on a current: the influence of vorticity, a sloping bed and
 900 dissipation. Series paper 12. Inst. of Hydrodyn. & Hydraulic Engng, Tech. University of Denmark.
- 901 Brown, S.A., Greaves, D.M., Magar, V. and Conley, D.C., 2016. Evaluation of turbulence closure
 902 models under spilling and plunging breakers in the surf zone. Coastal Engineering, 114, 177-193.
- 903 Buldakov, E., 2013. Tsunami generation by paddle motion and its interaction with a beach: Lagrangian
 904 modelling and experiment. Coastal Engineering 80, 83–94.
- 905 Buldakov, E., 2014. Lagrangian modelling of fluid sloshing in moving tanks. Journal of Fluids and
 906 Structures 45, 1–14.
- 907 Buldakov, E., Taylor, P.H., Eatock Taylor, R., 2006. New asymptotic description of nonlinear water
 908 waves in Lagrangian coordinates. Journal of Fluid Mechanics 562, 431–444.
- 909 Buldakov, E., Stagonas, D., Simons, R., 2015. Lagrangian numerical wave-current flume. 30th
 910 International Workshop on Water Waves and Floating Bodies, 12-15th April, Bristol, UK. Available
 911 at: http://www.iwwwfb.org/Abstracts/iwwwfb30/iwwwfb30_07.pdf.
- 912 Buldakov, E., Stagonas, D., Simons, R., 2017. Extreme wave groups in a wave flume: Controlled
 913 generation and breaking onset. Coastal Engineering 128, 75 – 83.
- 914 Chakrabarti, S.K., 1996. Shear current and its effect on fixed and floating structures. Adv. Coas. Ocean
 915 Eng. 2, 231-276.
- 916 Chaplin, J., 1996. On frequency-focusing unidirectional waves. Int. J. Offshore Polar Eng. 6 (2), 131–
 917 137.
- 918 Chen, L.F., Zang, J., Hillis, A.J., Morgan, G.C.J., Plummer, A.R., 2014. Numerical investigation of
 919 wave – structure interaction using OpenFOAM. Ocean Engineering 88, 91 – 109.
- 920 Chen, L.F., Zang, J., Taylor, P.H., Stagonas, D., Buldakov, E., Simons, R., 2016. Numerical
 921 investigation of unsteady hydrodynamic loads on a vertical cylinder in waves and sheared currents.
 922 31th International Workshop on Water Waves and Floating Bodies, 3rd-6th April, Plymouth, MI,
 923 USA. Available at: http://www.iwwwfb.org/Abstracts/iwwwfb31/iwwwfb31_05.pdf.
- 924 Christensen, E.D., Bredmose, H., Hansen, E.A., 2009. Transfer of Boussinesq waves to a Navier–Stokes
 925 solver. Application to Wave Loads on an Offshore Wind Turbine Foundation. Paper No.
 926 OMAE2009-79629, pp. 917-926.
- 927 Chen, L.F., Zang, J., Taylor, P.H., Sun, L., Morgan, G.C.J., Grice, J., Orszaghova, J. and Ruiz, M.T.,
 928 2018. An experimental decomposition of nonlinear forces on a surface-piercing column: Stokes-type
 929 expansions of the force harmonics. Journal of Fluid Mechanics 848, 42-77.
- 930 Christou, M., Ewans, K., 2014. Field measurements of rogue water waves. J. Phys. Oceanogr. 44 (9),
 931 2317–2335.
- 932 Courant, R., Friedrichs, K., Lewy, H., 1967. On the partial difference equations of mathematical physics.
 933 IBMJ. Res. Dev. 11(2), 215–234.
- 934 Drevard, D., Marcer, R., Grilli, S.T., Asce, M., Fraunie, P., Rey, V., 2005. Experimental validation of a
 935 coupled BEM-Navier–Stokes model for solitary wave shoaling and breaking. Ocean Waves
 936 Measurements and Analysis, Fifth International Symposium WAVES 2005, Madrid, pp. 1–10
- 937 Fernandez, H., Sriram, V., Schimmels, S., Oumeraci, H., 2014. Extreme wave generation using self-
 938 correcting method – revisited. Coast. Eng. 93, 15–31.
- 939 Ferziger, J.H., Perić, M., 2002. Computational Methods for Fluid Dynamics. 3rd ed. Berlin: Springer.
- 940 Fitzgerald, C., Taylor, P.H., Eatock Taylor, R., Grice, J., Zang, J., 2014. Phase manipulation and the
 941 harmonic components of ringing forces on a surface-piercing column. Proc. R. Soc. A. 470,
 942 20130847.

943 Forristall, G.Z., Cooper, C.K., 1997. Design current profiles using empirical orthogonal function (EOF)
944 and inverse FORM methods. In: Proceedings of the Offshore Technology Conference (OTC) 8267.
945 Offshore Technology Conference.

946 Gunn, K., Stock-Williams, C., 2013. On validating numerical hydrodynamic models of complex tidal
947 flow. *Inter. J. Mar. Energy* 3, e82 – e89.

948 Greenshields, C. J., 2015. OpenFOAM, The Open Source CFD Toolbox, Programmer’s Guide. Version
949 2.4.0. OpenFOAM Foundation Ltd.

950 Greenshields, C. J., 2015. OpenFOAM, The Open Source CFD Toolbox, User’s Guide. Version 2.4.0.
951 OpenFOAM Foundation Ltd.

952 Grue, J., 2002. On four highly nonlinear phenomena in wave theory and marine hydrodynamics. *Applied*
953 *Ocean Research* 24, 261 – 274.

954 Hirt, C.W., Nichols B.D., 1981. Volume of fluid (VOF) method for the dynamics of free boundaries. *J*
955 *Comput Phys* 39(1), 201–25.

956 Issa, R.I., 1986. Solution of the implicitly discretised fluid flow equations by operator-splitting. *J*
957 *Comput Phys* 62 (1), 40–65.

958 Jacobsen N.G., Fuhrman D.R., Fredsøe J., 2012. A wave generation toolbox for the open-source CFD
959 library: OpenFOAM. *Int J Numer Methods Fluids* 70(9), 1073–88.

960 Johannessen, T.B., Swan, C., 2001. A laboratory study of the focusing of transient and directionally
961 spread surface water waves. *Proc. R. Soc. Lond. A.* 457, 971 - 1006.

962 Jonathan, P., Taylor, P.H., 1997. On irregular, nonlinear waves in a spread sea. *Journal of Offshore*
963 *Mechanics and Arctic Engineering* 119 (1), 37-41.

964 Kirby, J.T., Chen, T.M., 1989. Surface waves on vertically sheared flows: Approximate dispersion
965 relations. *J. Geophys. Res.* 94, 1013-1027.

966 Kishida, N., Sobey, R.J., 1988. Stokes theory for waves on a linear shear current. *J. Eng. Mech.* 114,
967 1317 – 1334.

968 Ko, J., Krauss, W., 2008. Effect of vorticity on steady water waves. *J. Fluid Mech.* 608, 197 – 215.

969 Larsen, B.E., Fuhrman, D.R. and Roenby, J., 2018. Performance of interFoam on the simulation of
970 progressive waves. preprint arXiv:1804.01158.

971 Li, T., Troch, P., Rouck, J.D., 2007. Interactions of breaking waves with a current over cut cells. *J.*
972 *Comput. Phys.* 233, 865 – 897.

973 Markus, D., Hojjat, M., Wuechner, R., Bletzinger, K.U., 2013. A CFD approach to modeling wave-
974 current interaction. *Int. J. Offshore Polar Eng.* 23, 29 – 32.

975 Nwogu, O.G., 2009. Interaction of finite-amplitude waves with vertically sheared current fields. *J. Fluid*
976 *Mech.* 627, 179 – 213.

977 Park, J.C., Kim, M.H., Miyata, Y., 2001. Three-dimensional numerical wave tank simulations on fully
978 nonlinear wave-current-body interactions. *J. Mar. Sci. Technol.* 6, 70 – 82.

979 Paulsen, B.T., Bredmose, H., Bingham, H.B., 2014a. An efficient domain decomposition strategy for
980 wave loads on surface piercing circular cylinders. *Coastal Engineering* 86, 57-76.

981 Paulsen, B.T., Bredmose, H., Bingham, H.B., Jacobsen, N.G., 2014b. Forcing of a bottom-mounted
982 circular cylinder by steep regular water waves at finite depth. *J. Fluid Mech.* 755, 1–34.

983 Peregrine, D.H., Jonsson, I.G., 1983a. Interaction of waves and currents. *Advances in Applied*
984 *Mechanics* 16, 9 -117.

985 Peregrine, D.H., Jonsson, I.G., Galvin, G.J., 1983b. Annotated bibliography on wave-current interaction.
986 MR 83 -7, US Army, Corps of Engineers, Coastal Engineering Research Center, Fort Belvoir, VA.

987 Rapp, R.J., Melville, W.K., 1990. Laboratory measurements of deep-water breaking waves. *Philos.*
988 *Trans. Roy. Soc. Lond. A Math. Phys. Eng. Sci.* 331 (1622), 735–800.

989 Santo, H., Taylor, P.H., Bai, W. and Choo, Y.S., 2015. Current blockage in a numerical wave tank: 3D
990 simulations of regular waves and current through a porous tower. *Computers & Fluids*, 115, 256-269.

991 Santo, H., Stagonas, D., Buldakov, E., Taylor, P.H., 2017. Current blockage in sheared flow:
992 Experiments and numerical modelling of regular waves and strongly sheared current through a
993 spaced-frame structure. *Journal of Fluids and Structures* 70, 374 – 389.

994 Santo, H., Taylor, P.H., Day, A.H., Nixon, E., Choo, Y.S., 2018. Current blockage and extreme forces
995 on a jacket model in focussed wave groups with current. *Journal of Fluids and Structures* 78, 24-35.

996 Santo, H., Taylor, P.H., Eatock Taylor, R. and Choo, Y.S., 2013. Average properties of the largest waves
997 in Hurricane Camille. *Journal of Offshore Mechanics and Arctic Engineering*, 135(1), 011602-
998 011602-7.

999 Schmittner, C., Kosleck, S., Hennig, J., 2009. A phase-amplitude iteration scheme for the optimization
1000 of deterministic wave sequences. In: *Proceedings of the International Conference on Offshore*
1001 *Mechanics and Arctic Engineering*. Paper No. OMAE2009-80131, pp. 653-660.

1002 Smeltzer, B.K., Ellingsen, S.Å., 2016. Surface waves on arbitrary vertically-sheared currents. *Physics*
1003 *of Fluids* 29, 047102.

1004 Stacey, M.T., Monismith, S.G., Buran, J.R., 1999. Measurements of Reynolds stress profiles in
1005 unstratified tidal flow. *J. Geophys. Res.* 104, 10935 - 10949.

1006 Stagonas, D., Buldakov, E., Simons, R., 2014. Focusing unidirectional wave groups on finite water depth
1007 with and without currents. In: *Proceedings of the 34th International Coastal Engineering Conference*
1008 *(ICCE)*, Seoul, South Korea. Vol. 34, 1-7.

1009 Stagonas, D., Buldakov, E., Simons, R., 2018a. Experimental generation of focusing wave groups on
1010 following and adverse-sheared currents in a wave-current flume. *Journal of Hydraulic Engineering*,
1011 144(5), 04018016.

1012 Stagonas, D., Higuera, P., Buldakov, E., 2018b. Simulating breaking focused waves in CFD:
1013 methodology for controlled generation of first and second order. *J. Waterway, Port, Coastal, Ocean*
1014 *Eng.*, 144 (2), 06017005.

1015 Steer, J., Stagonas, D., Buldakov, E., Borthwick, A., van den Bremer, T., 2017. Stability of surface
1016 gravity waves on constant vorticity current. In: *Proceedings of 70th Annual Meeting of the APS*
1017 *Division of Fluid Dynamics*, 62 (14). *Bulletin of the American Physical Society*.

1018 Swan, C., Cummins, I.P., James, R.L., 2001a. An experimental study of two-dimensional surface water
1019 waves propagating on depth-varying currents. Part 1. Regular waves. *J. Fluid Mech.* 428, 273 – 304.

1020 Swan, C. and James, R.L., 2001. A simple analytical model for surface water waves on a depth-varying
1021 current. *Appl. Ocean Res.* 22, 331-347.

1022 Taylor, P.H., Williams, B.A., 2004. Wave statistics for intermediate depth water: new waves and
1023 symmetry. *J. Offshore Mech. Arct. Eng* 126(1), 54-59.

1024 Teles Da Silva, A., Peregrine, D.H., 1988. Steep, steady surface waves on water of finite depth with
1025 constant vorticity. *Journal of Fluid Mechanics* 195: 281-302.

1026 Thomas, G.P., 1981. Wave-current interactions: an experimental and numerical study. Part 1. Linear
1027 waves. *J. Fluid Mech.* 110, 457 – 474.

1028 Thomas, G.P., 1990. Wave-current interactions: an experimental and numerical study. Part 2. Nonlinear
1029 waves. *J. Fluid Mech.* 216, 505 – 536.

1030 Thomas, G.P., Klopman, G., 1997. Wave-current interactions in the nearshore region. In *Gravity waves*
1031 *in water of finite depth* (ed. J.N. Hunt), 215 – 319. *Computational Mechanics Publications*.

1032 Tromans, P.S., Anatrik, A., Hagemeyer, P., 1991. New model for the kinematics of large ocean waves
1033 application as a design wave. In: *Proceedings of the First International Offshore and Polar*
1034 *Engineering Conference*, pp. 64–71.

1035 Tsao, S., 1959. Behaviour of surface waves on a linearly varying flow. *Tr. Mosk. Fiz. – Tekh. Inst.*
1036 *Issled. Mekh. Prikl. Mat.* 3, 66 – 84.

1037 Vyzikas, T., Stagonas, D., Buldakov, E., Greaves, D., 2018. The evolution of free and bound waves
1038 during dispersive focusing in a numerical and physical flume. *Coastal Engineering*, 132, 95-109.

1039 Whittaker, C.N., Raby, A.C., Fitzgerald, C.J., Taylor, P.H., 2016. The average shape of large waves in
1040 the coastal zone. *Coastal Engineering*, 114: 253-264.

1041 Wroniszewski, P.A., Verschaeve, J.C., Pedersen, G.K., 2014. Benchmarking of Navier–Stokes codes
1042 for free surface simulations by means of a solitary wave. *Coastal Engineering* 91, 1-17.

1043 Wolf, J., Prandle, D., 1999. Some observations of wave-current interaction. *Coastal Engineering* 37 (3-
1044 4): 471-485.

1045 Yao, A., Wu, C.H., 2005. Incipient breaking of unsteady waves on sheared currents. *Physics of Fluids*
1046 17, 082104.

1047 Zang, J., Gibson, R., Taylor, P.H., Eatock Taylor, R., Swan, C., 2006. Second order wave diffraction
1048 around a fixed ship-shaped body in unidirectional steep waves. *J. Offshore Mech. Arct. Eng.* 128
1049 (2), 89–99.

- 1050 Zang, J., Taylor, P.H., Morgan, G., Stringer, R., Orszaghova, J., Grice, J., Tello, M., 2010. Steep wave
1051 and breaking wave impact on offshore wind turbine foundations – ringing re-visited. The 25th
1052 International Workshop in Water Waves and Floating Bodies, 9th-12th May, Harbin, China.
1053 Available at http://www.iwwwfb.org/Abstracts/iwwwfb25/iwwwfb25_52.pdf.
1054 Zhang, J.S., Zhang, Y., Jeng, D.S., Liu, P.L.F., C. Zhang, 2014. Numerical simulation of wave-current
1055 interaction using a RANS solver. Ocean Engineering 75, 157-164.